Astronomy & Astrophysics manuscript no. jekyll
October 30, 2017

Modelling the spectral evolution of Supernovae.

M. Ergon[1] and C. Fransson[1]

The Oskar Klein Centre, Department of Astronomy, AlbaNova, Stockholm University, 106 91 Stockholm, Sweden

To be submitted to Astronomy and Astrophysics.

ABSTRACT

We present JEKYLL, a new code for modelling of SN spectra and lightcurves based on Monte-Carlo (MC) techniques for the radiative transfer. The code assumes spherical symmetry, homologoues expansion and steady state for the matter, but is otherwise capabable of solving the time-dependent radiative transfer problem in non-local-thermodynamic-equilibrium (NLTE). The method used was introduced in a series of papers by Leon Lucy, and we have extended it to include non-thermal excitation and ionization as well as charge-transfer and two-photon processes. Macroscopic mixing of the material, known to occur in the SN explosion, is taken into account in a statistical sense using a method introduced by Anders Jerkstrand. To save computational power we use a diffusion-approximation solver in the inner regions, where the radiation field is thermalized. Except for a description of JEKYLL, we provide comparisons with the ARTIS and SUMO codes in the photospheric and nebular phase, respectively, which shows a good agreement in the calculated spectra as well as the state of the gas. We also provide an application to Type IIb SNe, by calculating the early evolution for a model previuosly found to give a good match to SN 2011dh in the nebular phase. Comparing to observations of SN 2011dh we find that both spectra and lightcurves are reasonably well reproduced, although there are also some clear differences. Comparing to results where NLTE was partly switched off as well as to previous results with the LTE-based HYDE code, we see strong effects of NLTE even on the bolometric lightcurve. This highlights the needs for full NLTE calculations when simulating the spectra and lightcurves of SNe.

Key words. supernovae: general

1. Introduction

Modelling the spectral evolution and lightcurves of supernovae (SNe) is crucial for our understanding these phenomena, and much effort has been put into this during the last 50 years. To achieve realistic results local thermodynamical equlibrium (LTE) can generally not be assumed, and the full frequency-dependent, non-LTE (NLTE) problem has to be solved. Several paths exist and the one followed here is the one outlined in a series of papers by Lucy (2002, 2003, 2005, herafter L02, L03, L05). Using this method, the radiative transfer is solved by a Monte-Carlo (MC) calculation, which is alternated with a NLTE solution for the matter until convergence is achieved (λ-iteration). Basic tests were performed in the original papers, and a simplified version of the method, assuming LTE for the population of excited states, has been implemented in the code ARTIS (Kromer & Sim 2009). Here we present JEKYLL, a C++ based code which implements the full NLTE-version of the method, extended to include also non-thermal excitation and ionization as well as charge-transfer and two-photon processes. These extensions are particulary important for modelling in the nebular phase, and for the calculation of the non-thermal rates we use the method developed by Kozma & Fransson (1992). Contrary to ARTIS, the intial version of JEKYLL is restricted to a spherical symmetric geometry, although the MC radiative transfer is performed in 3-D. In the paper, we present comparisons with ARTIS as well as the steady-state code SUMO (J11, herafter J11) aimed for the nebular phase. SUMO has NLTE-capabilities similar to JEKYLL, and together these two comparisons provide a critical test of mosts of the functionality of JEKYLL.

Type IIb SNe are thought to originate from stars that have lost most, but not all of their hydrogen envelope. Except for the prototypical Type IIb SN 1993J, the most well-observed Type IIb SN is 2011dh, for which we presented observations and modelling of the lightcurves in Ergon et al. (2014, 2015, hereafter E14, E15), as well as modelling of nebular spectra in Jerkstrand et al. (2015, hereafter J15). The modelling suggested a mass of $\sim$12 $M_\odot$ for the progenitor, a conclusion supported by observations of the star in pre-explosion images (Maund et al. 2011). As stellar winds for stars of this mass seems too low to expell the hydrogen envelope this points towards a binary origin, where the hydrogen envelope was lost through interaction with a companion star. A similar conclusion, based on modelling of the SN, pre-explosion observations of the progenitor star, as well as a likely post-explosion detection of the companion star, applies to SN 1993J. It is therefore of great interest to further explore the preferred 12 $M_\odot$ model presented in J15, evolved through the nebular phase using SUMO, and compared to the observed spectra and lightcurves of SN 2011dh in J15 and E15, respectively. This model was also evolved through the early phase using the hydrodynamical code HYDE in E15, allowing a comparison of the bolometric lightcurve with observations. Using JEKYLL we will be able to calculate the early spectral evolution, as well as the broadband and bolometric lightcurves in much greater realism, and compare to observations as well as to the results obtained with HYDE.

The paper is organized as follows. In Sect. 2 we discuss the underlying physical problem, and in Sect. 3 we describe the method used to solve this problem and the implementation of the code. In Sect. 4 we provide comparisons of JEKYLL to the ARTIS and SUMO codes. In Sect. 5 we apply the code to Type IIb SNe, calculates the early spectral evolution for the preferred J15 model, and discuss and compare the results to observations

of SN 2011dh. Finally, in Sect. 6 we conclude and summarize the paper.

2. Physics

The general physical problem adressed is the time-evolution of the radiation field and the state of the matter given the dynamical constraint of homologous expansion, and might be referred to as a radiation-thermodynamical problem. If the radiation field and the matter are in local thermodynamical equilibrium (LTE) this is simplified to a one-parameter (i.e the temperature) problem, and may be easily solved. Otherwise, we are in the non-LTE (NLTE) regime, and the number of parameters as well as the complexity of the problem increase drastically.

As is often done, we solve for the radiation field and state of the matter separately, and the problem is split into a radiative transfer and a thermodynamical part. The coupling, provided by radiation-matter interactions, is enforced through Λ-iterations, where the state of the matter and the radiation field are alternately and iteratively determined from each other. This concept is central to the method, and in Sect. 2.1 we provide some background and disuss the somewhat different meaning it has when using traditional or MC based methods.

The state of the matter can be split into a dynamical and thermodynamical part, where the former is trivially given by $\rho = \rho_0 \, (t/t_0)^3$ and $v = r/t$ through the constraint of homologous expansion. The thermodynamical part is given by the temperature, and the populations of ionized and excited states of the atoms, which are solved for using the thermal energy equation and NLTE rate equations, respectively. To simplify we assume steady state, which is motivated if the thermodynamical time-scale is much smaller than the dynamical time-scale.

The state of the radiation field is given by the specfic intensity, which is solved for using the MC method outlined by L02, L03 and L05, and discussed in 3.2. In a "traditional" code the specific intensity is solved for using the radiative transfer equation, whereas in a MC based code like JEKYLL, the radiative transfer is treated explicitly by propagating radiation packets which interacts with the matter through absorption, emission and scattering. The different radiation-matter interactions supported and their opacities and emissivities are discussed in 2.4.

2.1. Λ-iterations and convergence

In terms of the Λ-operator the radiative transfer equation may be written as $I = \Lambda[S]$, where I is the intensity and S the source-function. If the source function depends on the intensity, as in the case of scattering, solving the problem requires inverting the Λ-operator. This is typically a costly operation, and we may instead try an iterative procedure called Λ-iteration. In its original form an improved estimate of the intensity is then determined using the previous estimate of the source-function, i.e. $I_{i+1} = \Lambda[S_i]$. However, as has been extensively discussed in the literature, this method converges extremely slowly if the source function is dominated by scattering. This may be solved by splitting the Λ-operator in two parts, one acting on the current iterate and one acting on the previous iterate, i.e. $I_{i+1} = \Lambda^*[S_{i+1}] + (\Lambda - \Lambda^*)[S_i]$. With an appropriate choice of Λ^*, e.g the local part of Λ, which is trivial to invert and still close to Λ, convergence could be accelerated, and the procedure is therefore known as accelerated Λ-iteration.

It is important to realize that MC based Λ-iterations, unlike the original ones, does not suffer from slow convergence in the case of a scattering dominated source-function. The reason for this is that the scattering part of the problem is solved by the propagation of the MC packets.

2.2. Statistical equilibrium

To determine the populations of ionized and excited states of the atoms, the NLTE rate equations needs to be solved. Assuming steady state, these equations simplifies to the equations of statistical equilibrium, where the rate of transitions in and out of each state are in equlibrium. The statistical equilibrium equation for level i of ion I may be written

$$\sum_{J=I\pm1} \Lambda^{\mathrm{BF}}_{J,j\rightarrow I,i} \, n_{J,j} + \sum_{j\neq i} \Lambda^{\mathrm{BB}}_{I,j\rightarrow i} \, n_{I,j} = \left(\sum_{J=I\pm1} \Lambda^{\mathrm{BF}}_{I,i\rightarrow J,j} + \sum_{j\neq i} \Lambda^{\mathrm{BB}}_{I,i\rightarrow j} \right) n_{I,i} \tag{1}$$

where Λ is the transition rate (per particle) for bound-free (superscript BF) and bound-bound (superscript BB) transitions. Transitions may be caused by absorption or emission of photons or by collisions between ions and electrons (thermal or non-thermal). Transition rates for the supported radiative and collisional processes are discussed in 2.4 and 2.5, respectively.

2.3. Thermal equilibrium

To determine the thermal state of the gas the thermal energy equations needs to be solved. Assuming steady state, this equation simplifies to the equation of thermal equlibrium, where the heating and cooling of the gas are in equlibrium. The thermal equilibrium equation may be written

$$\sum_{J=I\pm1} g^{\mathrm{BF}}_{I,i\rightarrow J,j}(T) \, n_{I,i} + \sum_{i\neq j} g^{\mathrm{BB}}_{I,i\rightarrow j}(T) \, n_{I,i} + \sum g^{\mathrm{FF}}_{I}(T) = 0 \tag{2}$$

where $g = h - c$ is the net heating rate (per particle) for bound-free (superscript BF), bound-bound (superscript BB) and free-free (superscript FF) transitions. Heating/cooling may arise trough absorption/emission of photons, or through collisions involving ions and electrons (thermal or non-thermal). Heating/cooling rates for the supported radiative and collisional processes are discussed in 2.4 and 2.5, respectively.

2.4. Radiation-matter interactions

In radiation-matter interactions, the radiation field and the matter exchange energy through absorption and emission of photons. Except for electron scattering (Sect. 2.4.1), JEKYLL supports bound-bound, bound-free and free-free transitions discussed below in Sects. 2.4.2-2.4.4.

2.4.1. Electron scattering

Electron scattering is treated as coherent and isotropic in the comoving frame, in which case the opacity is given by the Thomson cross-section.

$$\kappa = \sigma_T \frac{n_e}{\rho} \tag{3}$$

where ρ is the density and n_e the electron number density.

2.4.2. Bound-Bound

An ion may transition between one bound state and another through absorption or emission of photons. The transitions are determined by their energy and their cross-sections, and assuming detailed balance the opacities and emissivities are related through the Einstein relations. We also assume that the Sobolov approximation apply, which is appropriate when the expansion broadening dominates the thermal broadening.

Optical depth The Sobolev optical depth for absorption in a transition from from level i of ion I is given by

$$\tau_{I,i\to u} = (B_{I,i\to u}\, n_{I,i} - B_{I,u\to i}\, n_{I,u}) \frac{hc}{4\pi} \frac{dr}{dv} \tag{4}$$

where $B_{I,i\to u}$ and $B_{I,u\to i}$ are the Einstein coefficients for absorption and stimulated emission, respectively, and $\frac{dr}{dv} = t$ in a homologously expanding ejecta.

Escape probability Is treated in the Sobolov approximation, and gives the probability for escape of a photon emitted in the transition with respect to self-absorption. The Sobolov escape probability for transition between level i and j of ion I is given by

$$\beta_{I,i,j} = \frac{1}{\tau_{I,j\to i}} (1 - \exp(-\tau_{I,j\to i})) \tag{5}$$

Emissivity In terms of the Sobolev escape probability, the emissivity for a transition from level i of ion I is given by

$$j_{I,i\to l} = \frac{h\nu}{4\pi} (A_{I,i\to l} + B_{I,i\to l}\, J_{I,i,l})\, \beta_{I,i,l}\, n_{I,i} \tag{6}$$

where $A_{I,i\to l}$ is the Einstein coefficient for spontaneous emission and $J_{I,i,l}$ the mean intensity at the transition frequency.

Transition rates In terms of the Sobolev escape probability, the upward and downward transition rates from level i of ion I are given by

$$\begin{aligned} R_{I,i\to l} &= A_{I,i\to l}\, \beta_{I,l,i} n_{I,i} \\ R_{I,i\to u} &= (B_{I,i\to u} n_{I,i} - B_{I,u\to i} n_{I,u})\, \beta_{I,i\to u} J_{I,u,i} \end{aligned} \tag{7}$$

Two-photon emissivity

2.4.3. Bound-Free

An ion may transition between a bound state and a free state (consisting of the next ion and a free electron), by absorption or emission of photons. The transitions are determined by their energy and their cross-sections, and assuming detailed balance the opacities and emissivities are related through the Milne relations.

Opacity In terms of the cross-section the opacity is given by $k_{I,i\to U,u}(\nu) = \sigma_{I,i\to U,u}(\nu)\, n_i$, where the cross-section is either determined from atomic data or from a simple hydrogenic approximation.

Emissivity Assuming detailed balance, the spontaneous and stimulated emissivity can be expressed in terms of the cross-section as

$$\begin{aligned} j^{\mathrm{SP}}_{I,i\to L,l}(\nu) &= \frac{h\nu}{4\pi}\, \phi_{I,i,L,l}(T)\, \sigma_{L,l\to I,i}(\nu)\, \frac{2h\nu^3}{c^2} e^{-\frac{kT}{h\nu}}\, n_{I,i}\, n_e \\ j^{\mathrm{ST}}_{I,i\to L,l}(\nu) &= \frac{h\nu}{4\pi}\, \phi_{I,i,L,l}(T)\, \sigma_{L,l\to I,i}(\nu)\, J(\nu)\, e^{-\frac{kT}{h\nu}}\, n_{I,i}\, n_e \end{aligned} \tag{8}$$

where $\phi_{I,i,L,l}(T) = n^*_{L,l}/n^*_{I,i}$, and the asterisk indicates the LTE value.

Transition rates In terms of the opacities and emissivities, the rates for upward and downward transition are given by

$$\begin{aligned} R_{I,i\to L,l} &= 4\pi \int_{\nu_0}^{\infty} \frac{1}{h\nu} \left(j^{\mathrm{SP}}_{I,i\to L,l}(\nu) + j^{\mathrm{ST}}_{I,i\to L,l}(\nu) \right) d\nu \\ R_{I,i\to U,u} &= 4\pi \int_{\nu_0}^{\infty} \frac{1}{h\nu}\, J(\nu)\, k_{I,i\to U,u}(\nu)\, d\nu \end{aligned} \tag{9}$$

Heating and cooling rates In terms of the opacities, emissivities and the transition rates the heating and cooling rates are given by

$$\begin{aligned} C_{I,i\to L,l} &= 4\pi \int_{\nu_0}^{\infty} \left(j^{\mathrm{SP}}_{I,i\to L,l}(\nu) + j^{\mathrm{ST}}_{I,i\to L,l}(\nu) \right) d\nu - h\nu_0\, R_{I,i\to L,l} \\ H_{I,i\to U,u} &= 4\pi \int_{\nu_0}^{\infty} J(\nu)\, k_{I,i\to U,u}(\nu)\, d\nu - h\nu_0\, R_{I,i\to U,u} \end{aligned} \tag{10}$$

2.4.4. Free-Free

With free-free transitions we refer to Brehmstralung, were both the initial and final states consists of a free electron and an ion. Assuming thermal Brehmstralung, the opacity and emissivity are related through Kirschoffs law.

Opacity and emissivity Assuming thermal emission the free-free emissivity for ion I is given by

$$j_I(\nu) = 6.8 \times 10^{-38}\, Z^2\, T^{-1/2}\, e^{-h\nu/kT}\, g_I\, n_I\, n_e \tag{11}$$

where Z is the charge of the ion and g_I is the gaunt factor, which we assume to be one. The free-free opacity for ion I may be expressed in terms of the emissivity using Kirschoffs law as $k_I(\nu) = j_I(\nu)\, B(T, \nu)$, where $B(T, \nu)$ is the blackbody intensity.

Heating and cooling In terms of the opacities and emissivities the heating and cooling rates for ion I are given by

$$\begin{aligned} C_I &= 4\pi \int_{\nu_0}^{\infty} j_I(\nu)\, d\nu \\ H_I &= 4\pi \int_{\nu_0}^{\infty} J(\nu)\, k_I(\nu)\, d\nu \end{aligned} \tag{12}$$

2.5. Matter-matter interactions

In matter-matter interactions, electrons and ions exchange energy through collisions. Collisions involving thermal and non-thermal electrons are discused in Sects. 2.5.1 and 2.5.2, respectively.

2.5.1. Thermal collisions

Collisions between thermal electrons and ions heats/cools the electron gas and results in bound-bound or bound free-transitions of the ions. If two ions are involved, electrons may be transferred between the ions, a process called charge-transfer.

Bound-bound rates Assuming detailed balance, the bound-bound transition rates can be expressed in terms of the collisional strength as

$$R_{I,i\to l} = q_{I,i\to l}\, n_{I,i}\, n_e = (\frac{2\pi\hbar^4}{kTm_e^3})^{1/2}\, \frac{1}{g_{I,l}}\, \Omega_{I,i\to l}(T)\, n_{I,i}\, n_e$$
$$R_{I,i\to u} = q_{I,i\to u}\, n_{I,i}\, n_e = \frac{q_{I,u\to i}}{\phi_{I,i,u}(T)}\, n_{I,i}\, n_e \quad (13)$$

where $\phi_{I,i,u}(T) = n^*_{I,i}/n^*_{I,u}$. and the asterisk indicates the LTE value. The heating and cooling rates are given by

$$H_{I,i\to l} = R_{I,i\to l}\, E_{I,i,l}, \;\; C_{I,i\to u} = R_{I,i\to u}\, E_{I,i,u} \quad (14)$$

Bound-free rates Assuming detailed balance, the bound-free transition rates can be expressed in terms of the collisional strength as

$$R_{I,i\to L,l} = q_{I,i\to L,l}\, n_{I,i}\, n_e = (\frac{2\pi\hbar^4}{kTm_e^3})^{1/2}\, \frac{1}{g_{L,l}}\, \Omega_{I,i\to L,l}(T)\, n_{I,i}\, n_e$$
$$R_{I,i\to U,u} = q_{I,i\to U,u}\, n_{I,i}\, n_e = \frac{q_{U,u\to I,i}}{\phi_{I,i,U,u}(T)}\, n_{I,i}\, n_e \quad (15)$$

where $\phi_{I,i,U,u}(T) = n^*_{I,i}/(n^*_{U,u}\, n_e)$, and the asterisk indicates the LTE value. The heating and cooling rates are given by

$$H_{I,i\to L,l} = R_{I,i\to L,l}\, E_{I,i,L,l}, \;\; C_{I,i\to U,u} = R_{I,i\to U,u}\, E_{I,i,U,u} \quad (16)$$

Charge-transfer rates In collisions involving two ions, electrons may be transfered from ion to another. This process is called charge-transfer and may be viewed as two bound-free transitions, although the process as a whole is rather bound-bound. The charge transfer rates may be expressed in terms of a charge-transfer coeffiecient that depends only on the temperature as

$$R_{I,i,J,j\to U,u,L,l} = \alpha_{I,i,j,j\to U,u,L,l}(T)\, n_{I,i}\, n_{J,j}$$
$$R_{U,u,L,l\to I,i,J,j} = \frac{\alpha_{I,i,J,j\to U,u,L,l}(T)}{\phi_{I,i,J,j,U,u,L,l}(T)}\, n_{U,u}\, n_{L,l} \quad (17)$$

where $\phi_{I,i,J,j,U,u,L,l}(T) = (n^*_{I,i}\, n^*_{J,j})/(n^*_{U,u}\, n^*_{L,l})$, and the asterisk indcates the LTE value. The energy difference between the initial and final state of the process give rise to heating or cooling of the electron gas with a rate given by

$$\alpha_{I,i,J,j\to U,u,L,l}\, (E_{I,i,L,l} - E_{J,j,U,u}) \quad (18)$$

2.5.2. Non-thermal collisions

Radioactive decays give rise to high-energy photons or leptons, which through a cascade of collisions with free and bound electrons give rise to a non-thermal high-energy tail of the otherwise Maxwellian electron distribution. The non-thermal electron distribution and the fractions of the energy going into heating, excitation and ionization of the gas can be calculated by solving the Spencer-Fano equation (Boltzman equation for electrons). This problem was solved by KF92 and for a further discussion we refer to this paper.

3. Method and implementation

The SN ejecta is represented by a grid of cells holding the local state of the matter and the radiation field. Homologous expansion is assumed, and although the implementation is mostly geometry independent, the current version only supports spherically symmetric cells. To update the state, JEKYLL provides several solvers with different levels of approximation (e.g. LTE and NLTE) for the matter, and a MC solver based on the method by (Lucy 2002, 2003, 2005) for the radiation field. Alternate updates of the matter and the radiation field constitutes a Λ-iteration, which is terminated when convergence is achieved. JEKYLL also provides a diffusion solver, intended for use at high optical depths where the matter and radiation field may be assumed to be in LTE. JEKYLL may be configured to run in steady-state or time-dependent mode, although steady-state breaks down at high optical depths where the diffusion time is large. The steady-state mode is therefore best suited for modelling in the nebular phase, or of the SN athmosphere in the photospheric phase.

3.1. Grid

The grid represents the SN ejecta, holds the atomic data and is spatially divided into a number of cells, in turn holding the local state of the matter and radiation field. The initial state is loaded in a generic way from file, specifying the number of cells, their spatial extent, and the local state of each cell. The grid also provides and option to export the state as well as a number of derived quantities (e.g. opacities and heating/cooling rates) to file, to be examined later or viewed in realtime by the specifically developed JEKYLL monitor.

3.1.1. Atomic data

The atomic data used by JEKYLL is loaded in a generic way from file, and may be collected from different sources. The data is organized in a hierarchical structure of atoms, isotopes and ions, specified by their proton, neutron and electron numbers, respectively. Each ion holds a list of bound states, as well as a list of bound-bound transitions between these states, and each atom holds a list of bound-free transitions between the bound states of their ions. The bound-bound transitions holds their spontaneus emission rates and collisional strengths, as well as their two-photon emission rates and frequency distributions (optional), whereas the bound-free transitions holds their radiative cross-sections and collisional strengths. In addition, it is possible to specify total as well as specific recombination rates for the ions, which might be used for a recombination correction. The atomic data also contins an (optional) list of charge-transfer reactions, which are mapped onto two bound-free transitions, one recombination and one ionization. The specific atomic data used

for the tests in Sects. 4.1 and 4.2 and for the application to Type IIb SNe in Sect. 5 are discussed separately in these sections.

3.1.2. Matter state

The local state of the matter in each cell is represented the density, the temperature and a hierarchical structure mirroring the atomic data, holding the massfractions of all isotopes and the number fractions of all ionized and excited states of each specie. Except for holding the local state, the responsibility of the cells is to provide functions for the solvers to calculate opacities and emissivities, as well as transition, heating and cooling rates based on the local state and the atomic data.

3.1.3. Radiation field

The local state of the radiation field in each cell is represented by the specific mean intensity and the flux at the cell borders, which are estimated and updated by the MC solver based on packet statistics following the method outlined by (Lucy 2003). Optionally, MC estimators for the specific intensity, the H and K angular moments, as well as the opacity and emissivity might be calculated. JEKYLL also supports a simplified radiation field model based on a diluted blackbody parametrization following the method outlined in (Mazzali & Lucy 1993), which is mainly intended for use together with the nebular matter-state solver.

3.1.4. Virtual cells

JEKYLL implements the concept of virtuall cells, representing clumpy and inhomogenous matter in a statistical sense. This method was introduced by Jerkstrand et al. (2011) to account for the macroscopic mixing of the nuclear burning shells on a grid otherwise spherical symmetric. Each cell may be divided into zones occupying some fraction (filling factor) of the cell volume, and otherwise geometrically unspecified. These zones may have different densities and compositions and the state solved for separately by the matter-state solver. With respect to the MC-solver the zones are represented by virtual cells differing only in a geometrical and statistical sence. The virtual cells are spherical, have a size corresponding to some number of clumps, and their location are randomly drawn during the MC radiative transfer based on their size and the zone filling factor.

3.2. MC solver

The radiation field is determined by the MC solver, where a number of radiation packets are propagated on the grid and interacts with the matter, which potentially change their energy, frequency and direction. The method used is similar to the one outlined in L02, L03 and L05, where indivisible and indestructible packets are propagated on a 3-D grid, but has been extended to include non-thermal ionizations and excitations as well as charge-transfer and two-photon processes. In addition, we introduce an alternative, more effiecient way to sample the emission frequency (Sect. 3.2.5), and a method to control the sampling of the radiation field (Sect. 3.2.6), allowing the packets to do work in the regions of freqeuency, space and time where they are actually needed. First, however, we describe the basic properties of the radiation packets, their creation, their propagation and their interaction with the matter (Sects. 3.2.1-3.2.4).

3.2.1. Packets

The radiation field is represented by packets, defined by their energy, frequency, position and direction. Following L03 and K09, we classify these as r-, i-, k- and g-packets, but further introduce e-packets to handle non-thermal processes. Freely propagating photons are represented by r-packets, and upon absorbed they may (temporarily) be converted into i- and k-packets, representing ionization/excitation and thermal energy, respectively. The g-packets are similar to the r-packets, but represents the γ-rays (or leptons) emitted in the radioactive decays, which are converted into e-packets upon absorption, and further into r-, i- or k-packets once one of the heating, ionization or excitation channels has been drawn.

3.2.2. Creation

The r-packets are created by sampling of the intensity, emissivity or luminosity of the radiation field, and the g-packets by sampling of the γ-ray (or lepton) emissivity. The packets may be created in several ways depending on the configuration and the type of problem solved. For example, when configured to run in steady-state using an inner blackbody boundary, the r-packets are sampled from the (one-sided) intensity at this boundary (specified by the temperature). On the other hand, in a time-dependent run the r-packets are initially sampled from the blackbody intensity of each cell (specified by the temperature), and then continously sampled from the luminosity at the inner boundary.

3.2.3. Propagation

After an interaction with the matter or a geometrical event the r-packet is ready to proceed its journey through the grid. If the previous event was an interaction a new random optical depth is drawn for the r-packet as

$$\tau = -\ln z, \tag{19}$$

and in either case distances to continuum and line interactions, as well as geometrical events are calculated. As the co-moving frequency is continously redshifted, all lines with a frequency lower (redder) than the r-packets co-moving frequency are checked sequentially, and if the accumulated optical depth exceeds the drawn value a line interaction is chosen. If, at any other point, the accumulated optical depth exceeds the drawn value a continuum interaction is chosen and, if the accumulated optical depth does not exceed the drawn value within the cell, a geometrical event is chosen. When the next event has been chosen the r-packet is moved to that location, its frequency and energy in the co-moving frame updated. In the case of an interaction, the packet is processed as described in Sect. 3.2.4, its frequency and energy in the rest-frame frame updated, and in either case progation continues as described above.

If the packet enters a cell containing virtuall cells, a randomly oriented virtual cell is drawn based on the filling factor of the corresponding zone. As long as the packet remains in the cell, the distance to the next geometrical event is given by the size and the orientation of the virtual cell, and at each border crossing the procedure is repeated.

3.2.4. Interactions

Once the packet has been absorbed, an emission event has to be drawn. In the case of scattering (electron or bound-bound), we assume that the frequency in the comoving frame does not change, and the packet is just re-emitted in a new direction drawn from an isotropic distribution. However, in the case of bound-bound, bound-free and free-free absorption, the frequency of the packet may change, and has to be drawn from the emissivity distribution. To achieve this we use the macro-atom method described by Lucy (2002, 2003), which enforce the constraints of energy conservation and statistical equilibrium on the radiation field. A complete description of this method is outside the scope of this paper, but as this is a key part of the MC solver a summary is motivated.

In bound-bound absorptions radiative energy is converted into excitation energy, and the r-packets are converted to i-packets. In free-free absorptions radiative energy is converted into thermal energy, and the r-packets are converted into k-packets. However, in bound-free absorptions radiative energy is partitioned into both ionization and thermal energy, and the r-packets are converted into either i- or k-packets based on the partitioning of the energy. The i-packets activates the macro-atom state-machine, involving transitions between all bound states of the specie, in turn de-activated by the choice of a radiative or collisional de-excitation. Radiative de-excitations corresponds to re-emission of the absorbed energy, the packet is converted back into a r-packet and a new frequency drawn based on the transition. Collisional de-excitations corresponds to conversion of the ionization/excitation energy into thermal energy, and the packet is converted into a k-packet. Based on the radiative and collisional cooling rates, k-packets are either converted into r-packets and re-emitted as thermal (bound-free or free-free) radiation, or converted back into i-packets, in which case a new macro-atom state-machine is activated by a collisional excitation. The power of the method is to reproduce the emissivity distribution given the aforementioned constraints, but the method is potentially ineffective, and in Sect. 3.2.5 we describe how to overcome this limitation.

In order to incorporate non-thermal excitation and ionization, the macro-atom method has to be slightly modified. Therefore, upon absorption, a g-packet is converted into an e-packet, representing the energy of the non-thermal electron distribution. Conversion into either k- or i-packets is then drawn based on the non-thermal heating, excitation and ioniation rates. Similarly, in the case of an i-packet the macro-atom state-machine is invoked by a non-thermal transition drawn based on the non-thermal excitation and ionization rates. The macro-atom state-machine is also modified by adding the probabilities for non-thermal transitions, which are always internal.

The macro-atom method also has to be modified to incorporate charge-transfer reactions. These are mapped on two bound-free transitions, one recombination and one ionization, and the treatment is somewhat similar to that of collisional bound-free transitions. Deactivation of the macro-atom state-machine through a charge-transfer recombination results in either re-activation through the corresponding ionization or, if the reaction is exo-thermic, in the conversion of the i-packet into a k-packet based on the energy released. Correspondingly, if the reaction is endo-thermic, k-packets may be transformed into i-packets based on the energy absorbed, and the macro-atom state-machine invoked by the corresponding ionization. The activations/deactivations of the macro-atom state-machine represents the transfer of ionization energy, whereas the conversions between i- and k-packets represent the thermal energy absorbed or released in the processs.

Finally, the method has to be modified to incorporate two-photon processes. This is achieved by adding the probabilities for (bound-bound) two-photon transitions to the macro-atom state-machine. Such transitions might be internal or de-activating, and in the latter case the emission frequency is drawn from the provided two-photon frequency distribution.

3.2.5. Markov-chain solution to the state-machine

A problem with the macro-atom method is that the number of transitions in the state-machine may become very large. This is particularly true when the collisional rates are high, causing the state-machine to bounce back and forth between macro-atoms and the thermal pool. To avoid this we use Markov-chain theory to calculate the probabilities to escape the state-machine by a de-activating transition. This approach can be applied to individual macro-atoms, or to the state-machine as a whole, consisting of all macro-atoms and the thermal pool. According to Markov-chain theory the average time spent in state i, given that the machine is envoked in state j, specified by the matrix $S_{i,j}$, can be calculated from the matrix $P_{i,j}$, containing the probabilities for internal transitions from state i to state j, through the relation $S^{-1} = P - I$. Knowing S, we may proceed to the state from which the machine will de-activate by a single draw, and once there, we may draw the de-activating transition from their (normalized) probabilities. This is implemented as two look-up tables for each bound state, one containing (a row of) S, and one containing the (normalized) de-activating transition probabilities. The matrix S has the size of the number of all bound states for all species plus one (the thermal pool), and the computational time to invert the matrix, which needs to be done once per Λ-iteration, as well as the look-up time in the tables, which needs to be done each time the state-machine is invoked, are potential problems.

3.2.6. Controlling the sampling of the radiation field

Another problem with the original method by Lucy is that there is no (or limited) control of the number of packets as a function of frequency, time and space. This may result in too few packets, leading to noise in the radiation field estimators, or too many, leading to unneccesary computational effort. To solve this we introduce a method for continuos resampling of the packets by letting their energy vary as a function frequency, space and time. This breaks the indivisibility requirement and, as we will see, the indesctrubility (energy conservation) requirement has to be modified to apply in an average sense.

A set of sampling regions (bounded in frequency, space and time) is defined, and each of these is assigned a packet energy. When packets cross the borders between sampling regions their energy is adjusted to that of the destination region. To maintain the rate of energy flowing across the borders, the rate of packets flowing across the borders has to be adjusted with the ratio of the packet energies in the source and destination regions (F). This is achived by adjusting all emission rates with 1/F and introduce a ficticious "emission" opacity (κ_E) corresponding to the total adjusted emission rate (which may be higher or lower than the original one). Athough the basic idea is simple, the actual implementation is complicated by the way the emission frequency is drawn in the macro-atom method.

Replacing κ with $max(\kappa, \kappa_E)$, packets are selected for either absorption, emission or both. The packet is absorbed with probability $max(\kappa/\kappa_E, 1)$ and emitted with probability $max(\kappa_E/\kappa, 1)$. If the packet is absorbed but not emitted it is terminated, and if the packet is emitted but not absorbed a child packet is created. Otherwise the transition is handled as described above (which also recovers the normal behavior if $\kappa = \kappa_E$). As is possible to show, this gives the correct (average) energy flows in and out of each sampling region. At spatial and temporal boundary crossings the packets are either split into F child packets (if F>1) or terminated with probability 1-1/F (if F<1).

3.3. LTE solver

The LTE solver determines the state of the matter assuming that LTE apply. The populations of ionized an excitated states are calculated using the Saha equations and the Boltzman excitation equation, respectively. The temperature may be set to the radiation temperature, estimated from the energy density or a diluted blackbody parametrization, or to the matter temperature determined by some other method.

3.4. Nebular solver

The nebular solver determines the state of the matter assuming that the radiative rates dominates, and is based on the approximations for the populations of ionized and excited states derived by Mazzali & Lucy (1993) and **?**. Following Mazzali & Lucy (1993), the temperature is assumed to be controlled by the radiation field and set to $0.9T_R$, where T_R is the temperature for a diluted blackbody paramatrization of the radiation field.

3.5. NLTE solver

This NLTE solver determines the state of the matter by solving the statistical and thermal equilibrium equations for the level populations and the temperature, respectively. The solution is determined in two steps. First the thermal equilibrium is scanned for in a configurable temperature intervall (based on the solution form a prevoius Λ-iteration), solving for statistical equilirium at each step. Based on this estimate, thermal and statistical equilibrium are simultaneosly iteratated for until convergence is achieved, using a procedure similar to what is described by Lucy (2003).

3.5.1. Statistical equilibrium

The non-linear statistal equilibrium equation system (Eq. 1) is solved by iteration on the level populations. In each step the system is linearized in terms of changes in the level populations, and the rates (per particle) are calculated using the previous estimate of these. The linearized system is then solved for the level populations using lower-upper (LU) decomposition and back-substitution. If all number derivatives (explicit and implicit) are included this is equivalent to a Newton-Raphson solver, but we leave this as a configurable choice, and in the simplest configuration only the explicit derivatives are included.

The equation system may be solved separately for the states of each atom, where any coupling terms needs to be dropped, or for all states at once. As the total number of states may be too large for a coupled solution, we also provide the possibility to alternate a decoupled solution with a fully coupled solution for the ionization balance. Typically a decoupled solution works well, but charge-transfer reactions and the source-function (used in the on-the-spot approximation) may introduce strong coupling terms. Transition rates for bound-bound and bound-free radiative and collisional processes (Eqs. 7, 9, 13 and 15), as well as for non-thermal, charge-transfer (Eq. 17) and two-photon processes are all supported, but which ones to include is a configurable choice.

3.5.2. Thermal equilibrium

The thermal equilibrium equation (Eq. 2) is solved either using the secant method (initial estmimate) or Newtons-Raphson's method (refined estimate), in which case a partial temperature derivative is used. Heating and cooling rates for bound-bound and bound-free radiative and collisional processes (Eqs. 10, 14 and 16), free-free processes (Eq. 12), as well as non-thermal and charge-transfer (Eq. 18) processes are all supported, but which ones to include is a configurable choice. In addition an expansion cooling term PdV/dt may also be included, as is motivated in a time-dependent run.

3.6. Mixing the solvers

JEKYLL also provides an option to mix the different matter state solvers. For example, the populations for species important for the ionization and heating-cooling balance may be solved for using the NLTE solver, whereas the populations for other species may be solved for using the LTE solver. Furthermore, it is also possible to determine the populations for ionized and excited states for a particular specie using different solver, e.g. solving for the ionization using the NLTE solver and for the excitation using the LTE solver, in a manner similar to what is done in ARTIS (and several other codes).

3.7. Non-thermal solver

The non-thermal solver determines the non-thermal electron distribution resulting from the radioactive decays, and the fraction of the deposited energy going into heating, excitation and ionizaton. This is done by solving the Spencer-Fano equation (i.e. the Boltzman equation for electrons) as described in KF92.

3.8. Diffussion solver

The diffusion solver determines the temperature in each cell by solving the thermal energy equation assuming spherical symmetry, homologous expansion, LTE and the diffusion approximation for the radiative flux. This results in a non-linear equation system for the temperature in each cell, which is solved by a Newton-Raphson like technique similar to the one used by Falk & Arnett (1977). Two specific topics requires some further discussion though; the Rosseland mean opacity used in the diffusion approximation and the outer boundary where the diffusion solver is supposed to be coupled to the MC solver.

3.8.1. Opacity

The Rosseland mean opacity used in the diffusion approximationis is calculated in a self-consistent way from the LTE state of the matter and the atomic data. This may sound like a straightforward calculation, but the bound-bound opacity and in particular, the virtual cell mode (see Sect 3.1.4) complicates it. In the latter case, if the clumps are all optically thin, the opacity may be

calculated as a zone average, but otherwise a geometrical aspect enters the problem, and the actual Rosseland mean might deviate considerably from one based on a zone-average.

Therefore we calculate the Rosseland mean opacity using an Monte-Carlo method, which is similar, but simpler and more efficient, than the one used for the radiative transfer. In each cell a large number of packets are sampled based on the blackbody flux distribution and the zone filling factors. These packets are then followed until they are absorbed, and their pathlength averaged to get the Rosseland mean free path. This gives the Rosseland mean opacity, including the bound-bound contribution as well as the geometrical effects arising in a clumpy material

3.8.2. Outer boundary

If the diffusion solver is coupled to an MC solver at the outer boundary, which is the main purpose of it, appropriate boundary conditions must be specified for both the diffusion and the MC solver. As outer boundary condition for the diffusion solver we use the temperature, and as inner boundary condition for the MC/NLTE solver we use the luminosity. To implement the latter condition we use an approximate method, where packets with total energy $L\Delta t$, sampled from a blackbody distribution at the local temperature are injected at the inner boundary, whereas MC packets propagating inwards are simply reflected at this boundary.

4. Comparisons

4.1. Comparison with ARTIS

Here we compare JEKYLL with ARTIS, a spectral synthesis code aimed for the photospheric phase presented in K09. Both ARTIS and JEKYLL are based on the method outlined in L02-L05, but ARTIS has a simplified NLTE treatment, where the bound states of the ions are assumed to be populated according to LTE and the energy deposited by the radioactive decays are assumed to be fully thermalized. On the other hand, JEKYLL assumes spherical symmetric geometry, which is not a limitation in ARTIS. We have made a reasonable effort to synchronize the atomic data, and to configure JEKYLL to run in a mode as similar to ARTIS as possible. For the comparison we use the Type IIb model 12C from J15, which is also used in the comparison with SUMO (Sect. **??**) and in the application to Type IIb SNe (Sect. 5). Note that ARTIS do not support non-thermal excitation and ionization, which is crucial for the population of the excited states of He I. Therefore, the setup used for the comparision will not be able to reproduce the He I signature characteristic of Type IIb (and Ib) SNe. However, this is not a problem for the comparision, which will provide a critical test of the MC raditative transfer as well as most of the methods used. However, the full NLTE capabilities of JEKYLL can not be tested here, and this is instead achieved thorugh the comparison with SUMO in Sect. 4.2.

Figures 1 and 2 shows the bolometric lightcurve and the spectral evolution, respectively, for model 12C as calculated with ARTIS (black) and JEKYLL (red). Clearly, as far as the observational quantities are concerned, the calculations seems to agree well.

4.2. Comparison with SUMO

Here we compare JEKYLL with SUMO, a spectral synthesis code aimed for the nebular phase presented in J11. Similar to

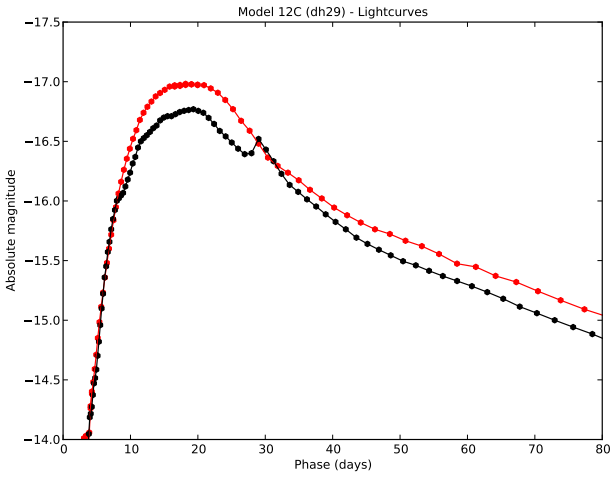

Fig. 1. Comparison of bolometric lightcurve for model 12C (J15) as calculated with ARTIS (black) and JEKYLL (red).

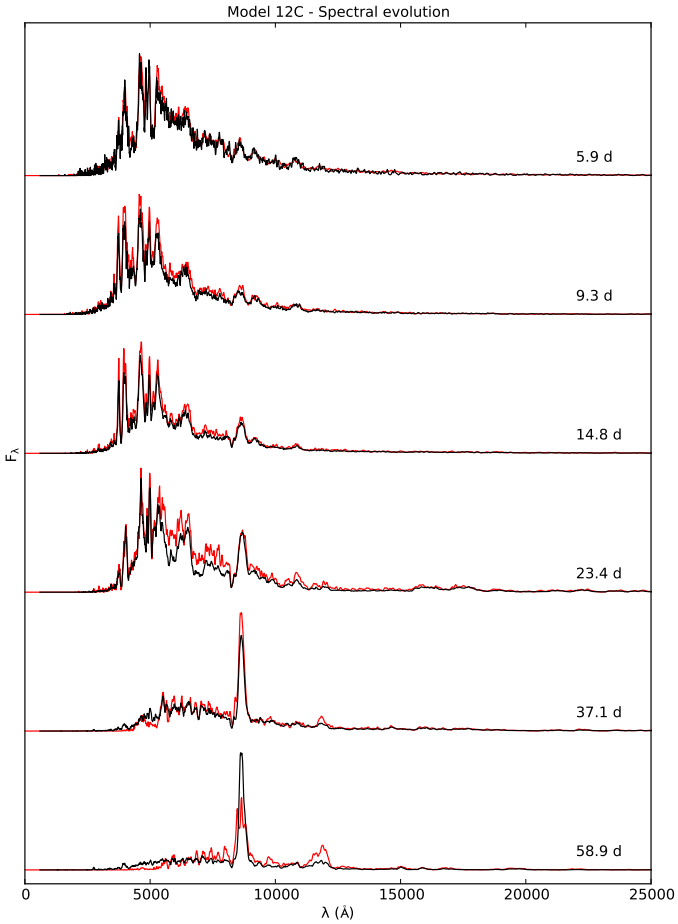

Fig. 2. Comparison of spectral evolution for model 12C (J15) as calculated with ARTIS (black) and JEKYLL (red).

JEKYLL, it uses a λ-iteration scheme, where the radiative transfer is solved with a Monte-Carlo method and state of the gas determined from statistical and thermal equalibrium. We have made a reasonable effort to synchronize the atomic data, and to configure JEKYLL to run in a mode as similar to SUMO as possible. For the comparison we use model 13G from the set of

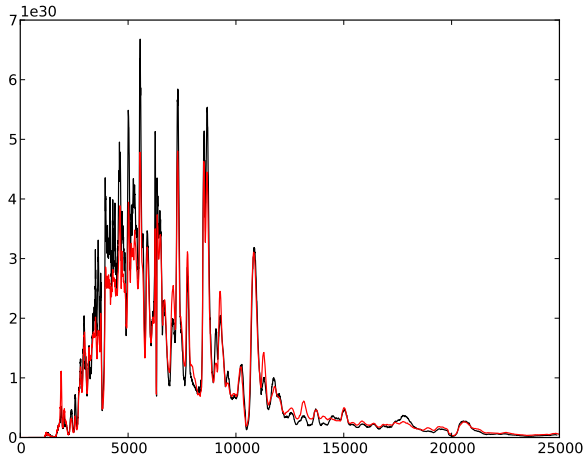

Fig. 3. Comparison of spectra for model 13G (J15) at 100 days as calculated with SUMO (black) and JEKYLL (red).

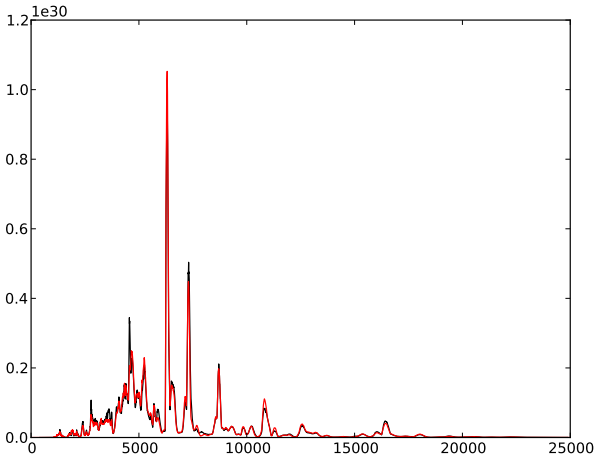

Fig. 5. Comparison of spectra for model 13G (J15) at 300 days as calculated with SUMO (black) and JEKYLL (red).

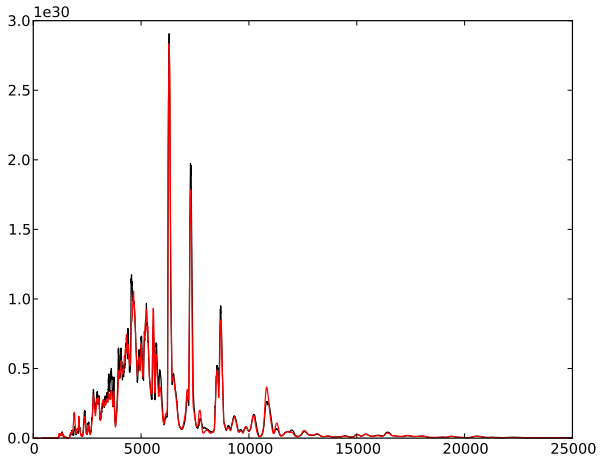

Fig. 4. Comparison of spectra for model 13G (J15) at 200 days as calculated with SUMO (black) and JEKYLL (red).

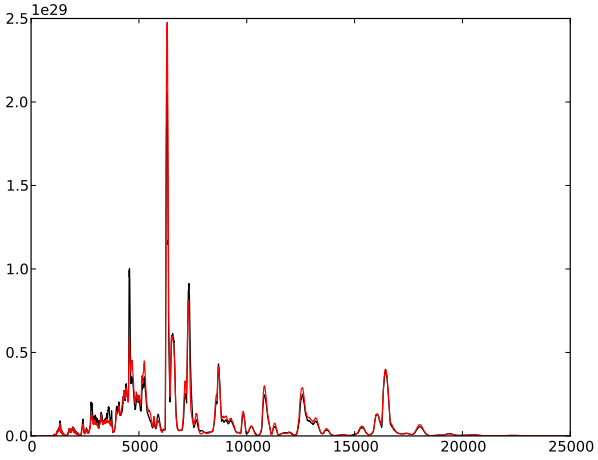

Fig. 6. Comparison of spectra for model 13G (J15) at 400 days as calculated with SUMO (black) and JEKYLL (red).

Type IIb models presented in J15, and run JEKYLL in steady-state mode at 100, 200, 300, 400 and 500 days. The spectral comparisons are shown in Figs. 3-7, and in Figs. 8 and 9 we show comparisons of the evolution of the temperature and the electron fraction, respectively.

As can be seen the specral agreement is quite good, altough the match is slightly worse at 100 and 500 days. The evolutin of the temperature shows a good agreement, except for the He/N and H zones at early times, whereas the evolution of the electron density shows a slightly worse agreement. In general the agreement at early (100-150 days) times is worse than later on, which is not surprising as some approximations made by SUMO are better suited for later phases. Given that the data and methods are not entirely synchronized the general agreement appears to be good and confirms that JEKYLL is working properly.

5. Application to Type IIb SNe

In J15 a set of Type IIb models differing in initial mass, mixing and a number of other parameters where introduced and evolved

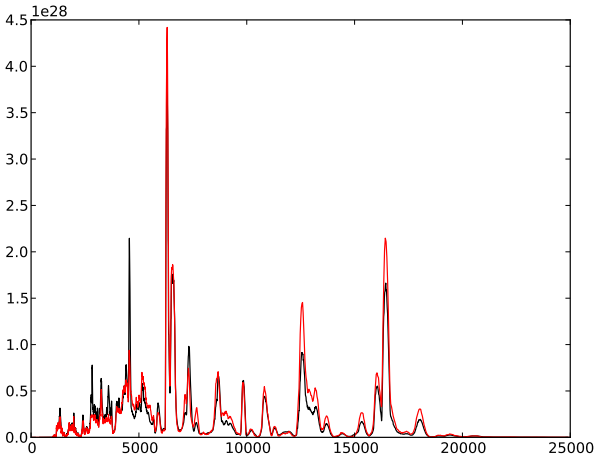

Fig. 7. Comparison of spectra for model 13G (J15) at 500 days as calculated with SUMO (black) and JEKYLL (red).

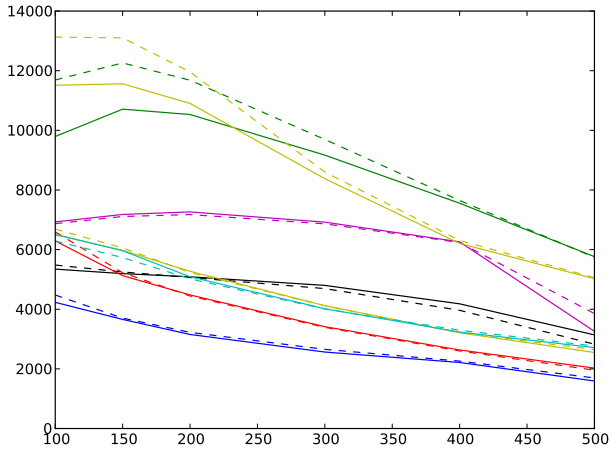

Fig. 8. Comparison of the evolution for the temperature for model 13G (J15) as calculated with SUMO (black) and JEKYLL (red).

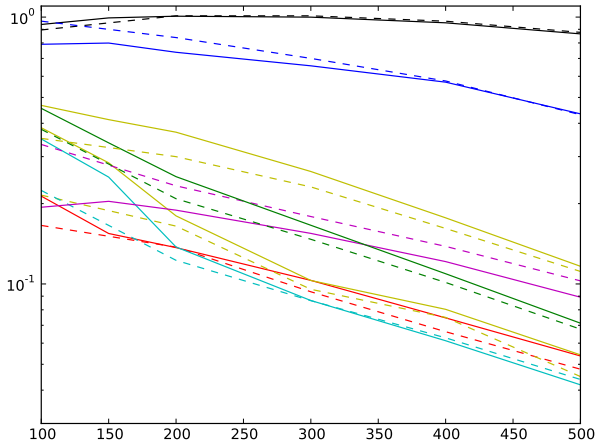

Fig. 9. Comparison of evolution of the electron fraction for model 13G (J15) as calculated with SUMO (black) and JEKYLL (red).

through the nebular phase. Among those, model 12C[1], which has an initial mass of 12 $M_\odot$, and strong mixing, was found to give the best match to the observed nebular spectra (J15) and lighcurves (E15) of SN 2011dh. It is therefore of great interest to explore how well this model reproduce the early spectra and lightcurves, something which is now possible using JEKYLL. The early bolometric lighcurve was modelled in E15 using the hydrodymamical, LTE-based code HYDE[2], and we can now investigate how well this simplified approach compares with a full NLTE calculation. It is also worth comparing to the NLTE models of stripped envelope (SE; Type IIb, Ib and Ic) SNe presented by Dessart et al. (2015, 2016). Those models where evolved with CMFGEN and in particular the Type IIb model 3p65Ax1 share many properties with model 12 C.

In Sect. 5.1 we describe model 12C and in Sects. 5.2, 5.3, 5.4 and 5.5 we discuss its spectral, photometric, colour and bolometric evolution and compare to observations of SN 2011dh. We

[1] Model 12F, preferred in E15, differs from model 12C only in the optical depth of the dust.

[2] Set up to run in homologous mode

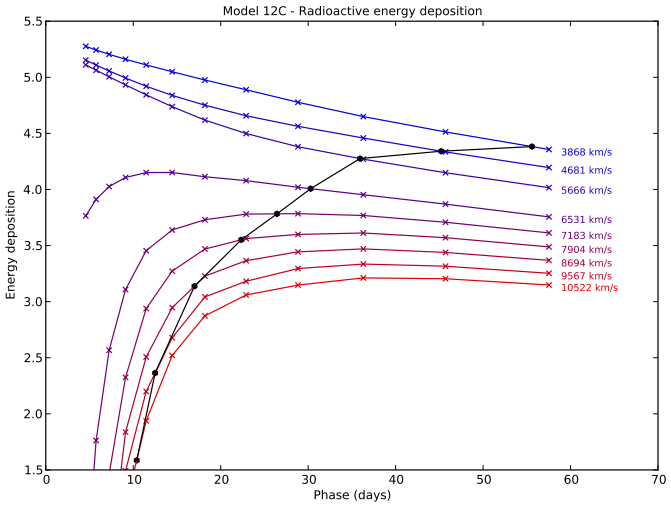

Fig. 11. Evolution of the radioactive energy deposition in the helium envelope for model 12C (J15).

will also discuss the physical processes giving rise to the observed evolution and in Figs. 10 and **??** we show the evolution of the basic matter and radiation quantities in model 12C. The former shows the evolution of the temperature, electron fraction, radioactive energy deposition as well as the photospheric radius, whereas the latter shows the evolution of the J, H and K moments of the radiation field, as well as the Eddington factor. Finally, in Sects. 5.6 and 5.7 we will discuss the effects of NLTE and macroscopic mixing on the calculated spectra and lightcurves.

5.1. Model description

A full description of model 12 C was given in J15, but we repeat the basic properties here. The masses and abundances for the Carbon-Oxygen core and the Helium envelope are adopted from a stellar evolutionary model by Woosley & Heger (2007) with an initial mass of 12 $M_\odot$, including also the yields from the explosive nucleosyntheis. The Carbon-Oxygen core is assumed to have a constant density, and the Helium envelope to have the same density profile as model He4R270 by Bersten et al. (2012). In addition, a 0.1 $M_\odot$ hydrogen envelope based on models by Woosley et al. (1994) was attached. The velocities of the intefaces between the Carbon-Oxygen core, the Helium envelope and the Hydrogen envelope where set to 3500 and 11000 km/s, respectively based on observations of SN 2011dh.

Based on the original onion-like nuclear burning structure, five compositional zones (O/C, O/Ne/Mg, O/Si/S, Si/S and Fe/Co/He) where identified in the Carbon-Oxygen core, and two compositional zones (He/N and He/C) where identified in the Helium envelope. To mimic the mixing of the nuclear burning zones in the explosion due to hydrodynamical instabilities, two scenarios with different degrees of mixing (medium and strong) where explored in J15. Of those, the strong mixing scenario used for model 12 C corresponds to a fully mixed Carbon-Oxygen core and about half of the radioactive Fe/Co/He material mixed into the inner part of the Helium envelope. As in J15 we take the macroscopic nature of the mixing into account using the virtual cell method (Sect. 3.1.4), but we have also run a model with microscopic mixing by just averaging the abundances in the different compositional zones. This method is used for the CMFGEN models by Dessart et al. (2015, 2016) as well as in many other works and therefore a comparison is highly motivated.

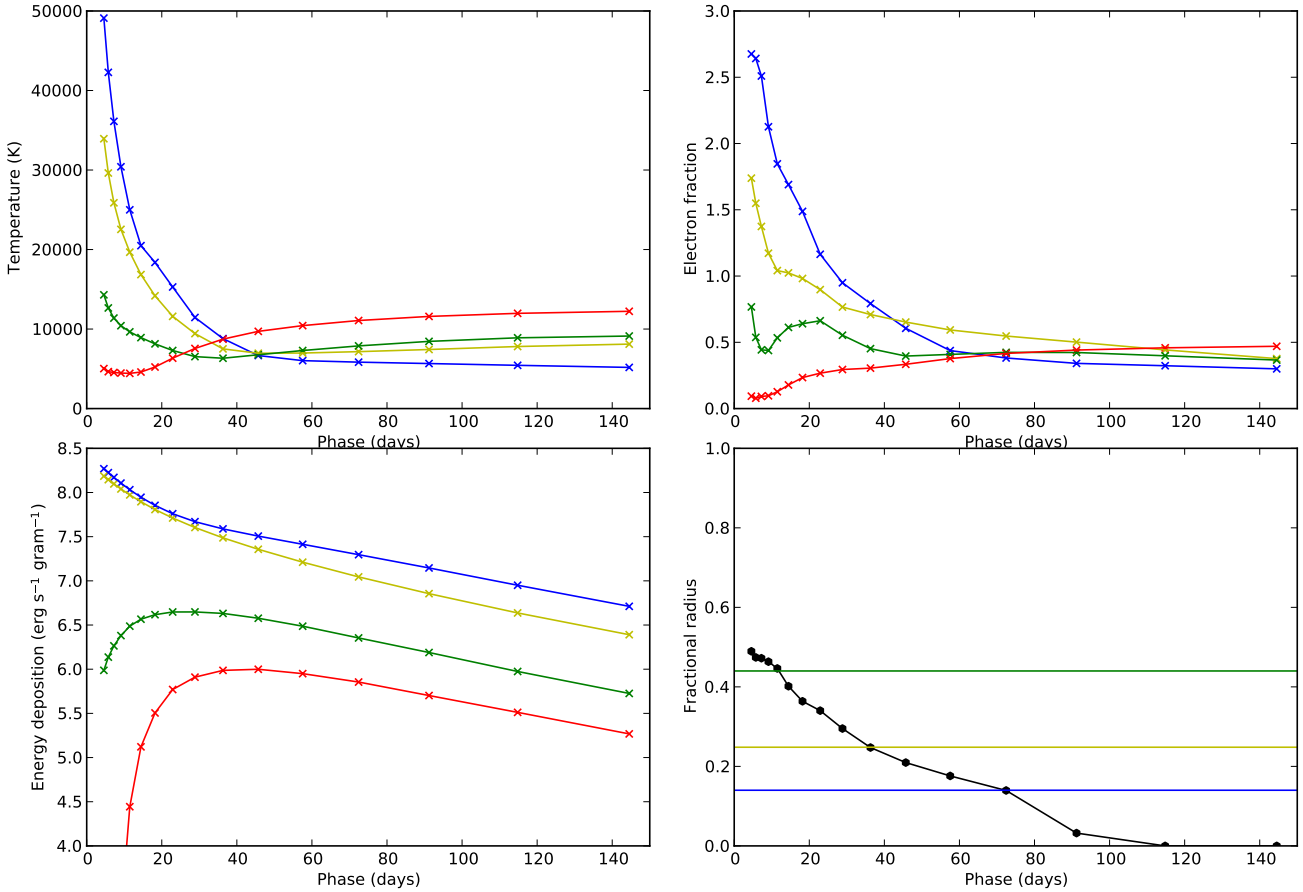

Fig. 10. Evolution of the temperature (upper left panel), electron fraction (upper right panel) and radioactive energy deposition (lower left panel) in the oxygen core (blue), inner/outer (green/yellow) helium envelope and the hydrogen envelope (red) for model 12C (J15). In the lower right panel we show the evolution of the photospheric radius as well as the outer borders of the carbon-oxygen core and inner/outer (green/yellow) helium envelope.

As for the HYDE models in E15, the model was evolved from 1 day with the initial temperature profile taken from the best-fit hydrodynamical model for SN 2011dh from that paper. This SN model was based on a bare helium core model, and therefore the cooling of the thermal explosion energy, lasting for a few days in a model with a hydrogen envelope, is ignored. As mentioned in E15, the subsequent evolution is powered by the continuous injection of radioactive decay energy, and the choice of initial temperature profile is not critical, although it may affect the early evolution to some extent.

The atomic data used is the same as for the comparison with SUMO (Sect. 4.2), but whith the following modifications. The highest ionization stage where increased to VI for all species, and the stage III ions where updated to include at least 50 levels for elements lighter than Sc, and at least 200 levels for heavier elements, using online data provided by NIST[3] and R. Kurucz[4]. Total recombination rates for the stage III ions were adopted from the online table provided by S. Nahar[5] whenever available, and otherwise from Shull & van Steenberg (1982). For ionization stages IV to VI we only included the ground-state multiplets, adopted the photo-ionization cross-section by (Verner & Yakovlev 1995; Verner et al. 1996) and assumed the populations to be in LTE with respect to stage IV.

[3] www.nist.gov
[4] http://www.cfa.harvard.edu/amp/ampdata/kurucz23/sekur.html
[5] http://www.astronomy.ohio-state.edu/~nahar/_naharradiativeatomicdata

5.2. Spectral evolution

Figure 13 and 14 show the spectral evolution for model 12C between 0 and 150 days, where the former displays the process, and the latter the location giving rise to the emission. Furthermore, in Fig. 12 we compare the spectral evolution in the optical and NIR to observations of SN 2011dh. As seen in Fig. 12, there is a good qualitative, and in many aspects also quantitative agreement, between model 12C and the observations of SN 2011dh. Before ~10 days, when the emission comes mainly from the hydrogen envelope the agreement is a bit worse (not shown). This is possibly an effect of the choice of initial conditions for the model (see Sect. 5.1), where the initial cooling of the explosion energy, lasting a few days, have been ignored.

The main signature of a Type IIb SNe is the transition from a hydrogen to a helium dominated spectrum, and this is well reproduced by the model. Initially, Hα in the optical and the Paschen-series in the near-infrared (NIR) are strong in the model and emission from the hydrogen envelope is dominating. Already at ~10 days emission from the helium envelope starts to dominate redwards ~5000 Å, and between 10 and 15 days the helium lines appears, grow stronger, and eventually dominates the spectrum at ~40 days. In the model, Hα and Pashen-line emission disappaers on a similar timescale, completing the transition, although Hα remains considerably longer in absorption. The first 40 days is also the period over which the contribution

from continuum processes fades away. Initially, this contribution is substantial redwards ∼5000 Å and dominating in the NIR, but then quickly fades away although it remains important in the *H*-band region and redwards 23000 Å until ∼40 days.

After ∼40 days, emission from the Carbon-Oxygen core becomes increasingly important and at ∼100 days it dominates redwards ∼5000 Å. As a consequence emission from heavier elements abundant in the core increase, in particular after ∼100 days when the strong forbidden lines from Oxygen and Calcium appears. This is also the moment when the Carbon-Oxygen core becomes fully transparent, at least in the continuum (see Fig.10), and therefore marks the transition into the nebular phase. This transition, initself a demanding test of the code, is quite nicely reproduced by the model. As discussed in Sect. 5.7, this is partly thanks to our treatment of the macroscopic mixing.

Below, we discuss in some more detail the emission from lines of Hydrogen (Sect. 5.2.1), Helium (Sect. 5.2.2), Carbon-Calcium (Sect. 5.2.3), Scandium-Manganese (Sect. 5.2.4) and Iron-Nickel (Sect. 5.2.5) and compare to observations of SN 2011dh. Finally in Sect. 5.2.6, we discuss the line velocities as measured from their absorption minimum and again compare to observations of SN 2011dh.

5.2.1. Hydrogen

The contribution from Hydrogen lines to the model spectrum is shown in Fig. 13, and as mentioned it is intially strong, but quickly fades away after ∼10 days, when the photosphere retreats into the increasingly transparent helium envelope (see Figs. 10 and 14). This is also the moment when most of the Hydrogen in the envelope have recombined, and therefore the recombination driven Pashen lines, which are initially strong, quickly dissappears (although Pashen α is still present at ∼25 days). The Balmer line emission dissapears on a similar timescale, whereas the absorption remains for a longer time as the 2s level these lines originate from is also populated by other means. Contrary to the other Balmer lines, Hα initially shows a clear P-Cygni profile, but after ∼10 days it becomes increasingly blended with the He I 6678 Å line and attains the double-peaked shape so characteristic of Type IIb SNe. Figure 15 shows the evolution of the Balmer lines as compared SN 2011dh. The evolution is qualitatively similar, but the absorption is significantly stronger and remains longer in the model, suggesting the ∼0.05 $M_\odot$ of hydrogen in the model to be larger than for SN 2011dh. This is in line with the 0.02-0.04 $M_\odot$ of hydrogen estimated by modelling of SN 2011dh in E14[6]. Also in agreement with this modelling, we find that the absorption minimum of the Balmer lines asymptotically approach the velocity of the hydrogen/helium envelope interface. This is also seen in Fig. 21, where we show the evolution of the absorption minimum of the Hα, He I 5876, 10830 and 20581 Å, and Fe I 5018 Å lines, as well as the Rosseland mean photosphere.

5.2.2. Helium

The contribution from Helium lines to the model spectrum is shown in Fig. 13, and as mentioned it increases strongly between 10 and 15 days, dominates the spectrum between 20 and 60 days and thereafter fades away in the optical but remains important in the NIR. Figures 16 and 17 shows the evolution of the optical (He I 5876 Å, 6678 Å and 7065 Å) and NIR (He I 10830 Å, 17007 Å and 20581 Å) Helium lines as compared to SN 2011dh. The He I 6678 Å and 20581 Å lines belongs to the singlet branch and the others to the triplet branch of He I ion, ending at the meta-stable $2s^1S$ and $2s^3S$ levels, respectively, which are directly linked to the ground state. The He I 5876 Å, 6678 Å and 10830 Å lines are quite well reproduced by the model, whereas the He I 7065 Å and 20581 Å lines seems to be a bit overproduced, and the weaker He I 17007 Å line (mainly seen in emission) is considerably stronger than in the observed spectra. We note, that the He I 20581 Å line is particularly sensitive to non-thermal excitation (Jerkstrand et al. 2015; Dessart et al. 2012), so the overproduction of this line could indicate that the mixing of the radioactive Fe/Co/He material is too strong. Note also, that after ∼50 days, most of the He I 5876 Å line emission begin to scatter into in the Na I 5890,5896 Å line.

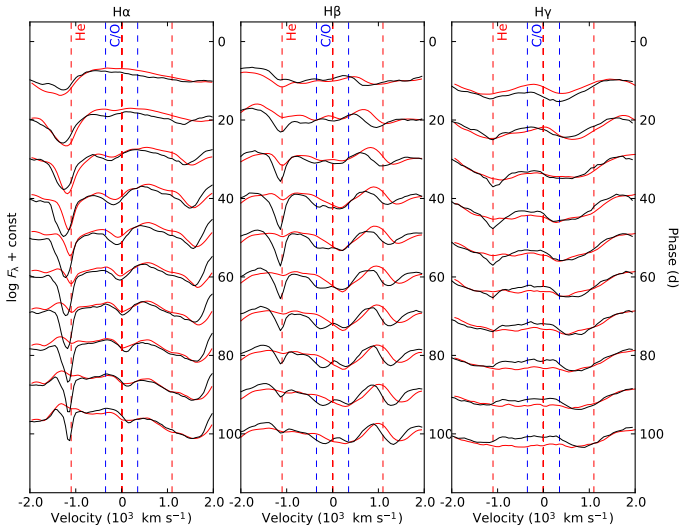

Fig. 15. Evolution of hydrodogen lines for model 12C as calculated with JEKYL (black) compared to the observations of SN 2011dh (red). Spectra from 10 equally spaced epochs between 10 and 100 days are shown, where those of SN 2011dh have been interpolated as decribed in E14. Here, as well as in Figs. 16-20, we also show the velocity extent of the He envelope (red lines) and the C/O core (blue lines).

As seen in Fig. 17 as well as Fig. 21, the absorption-minimum of the He I 10830 Å line appears near the photosphere and moves outward in velocity until ∼40 days. As discussed in E14, a similar behaviour is observed in SN 2011dh, although in this case also other helium lines showed a similar, but less pronounced trend. In E14 we suggested that the appearence and subsequent evolution of the helium lines was driven mainly by the ejecta becoming optically thin to the γ-rays. This idea is supported by Fig. 11, which shows the evolution of the radioactive energy deposition in the helium envelope. Between 10 and 15 days we see a strong increase in the energy deposition outside the photosphere, corresponding well to the appearence and increasing strength of the helium lines. We also see that the energy deposition in the outermost helium layers continues to increase to ∼40 days, which may explain the evolution of the He I 10830 Å line. The outward migration of the absorption of the He I 10830 Å line is also present in the Type I/IIb-like models by Dessart et al. (2015, 2016), and was noted and discussed by the authors, which also suggest a similar explanation.

[6] Using an early version of JEKYLL assuming steady-state, LTE and scattering only.

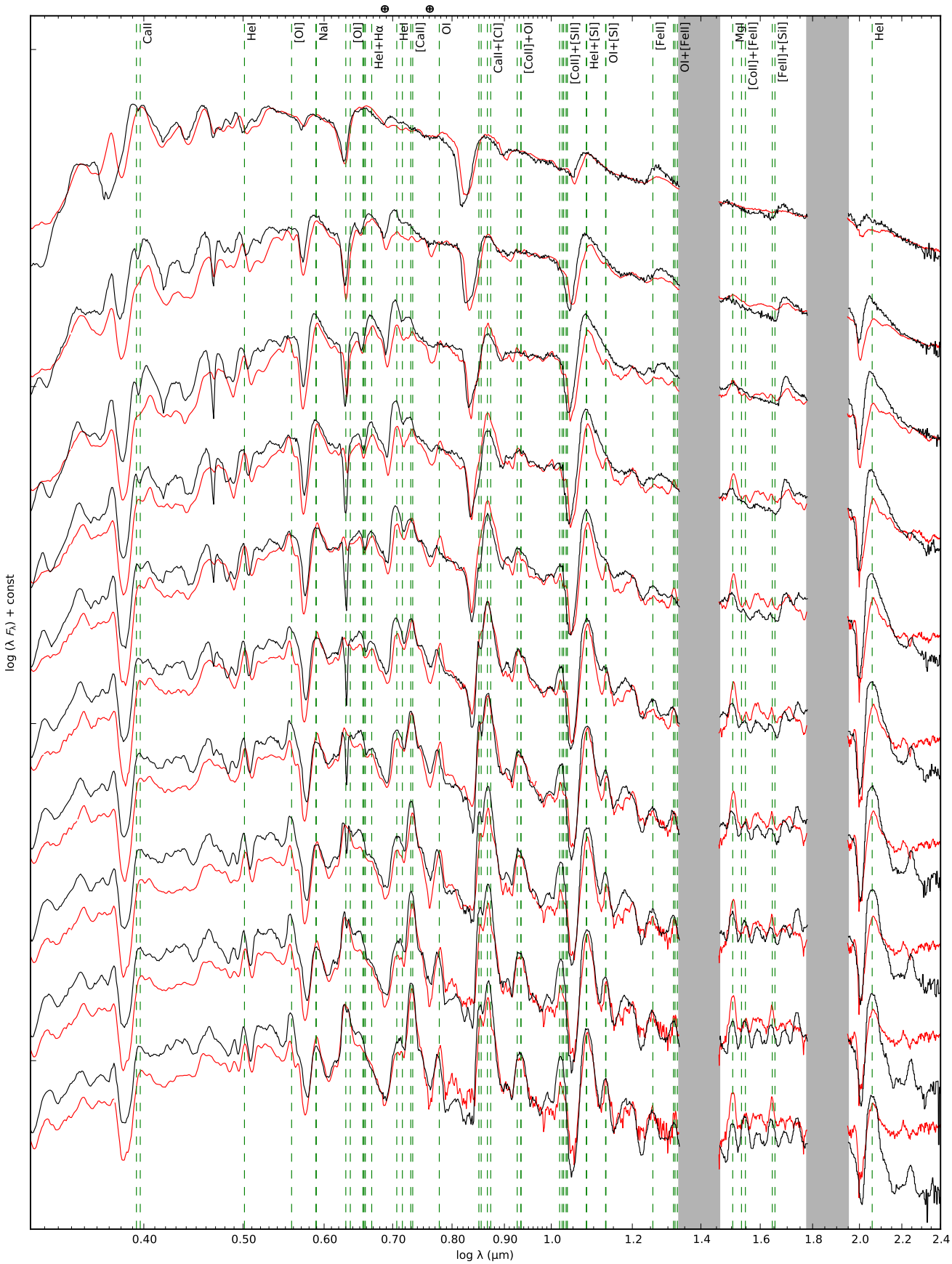

Fig. 12. Spectral evolution for model 12C as calculated with JEKYLL compared to the observations of SN 2011dh (red). Spectra from 10 equally spaced epochs between 15 and 150 days are shown, where those of SN 2011dh have been interpolated as decribed in E14.

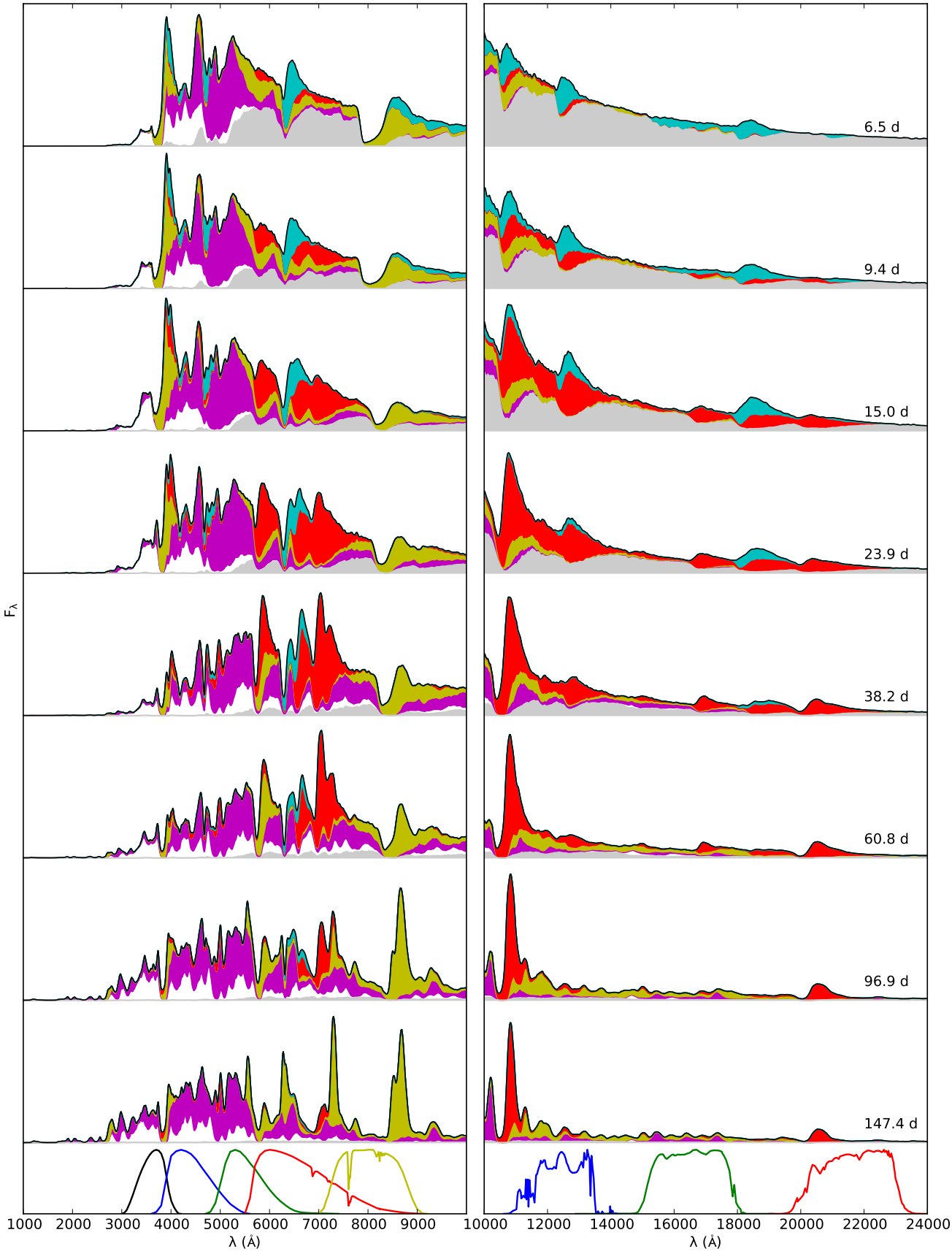

Fig. 13. Spectral evolution in the optical (left panel) and NIR (right panel) for model 12C as calculated with JEKYLL. In the spectra we show the contributions to the emission from bound-bound transitions of Hydrogen (cyan), Helium (red), Carbon-Calcium (yellow), Scandium-Manganese (white) and Iron-Nickel (mangenta) as well as continuum processes (grey). At the bottom we show the transmission profiles of the optical Johnson-Cousine *U* (black), *B* (blue), *V* (green), *R* (red) and *I* (yellow) bands and the NIR 2MASS *J* (blue), *H* (green) and *K* (red) bands.

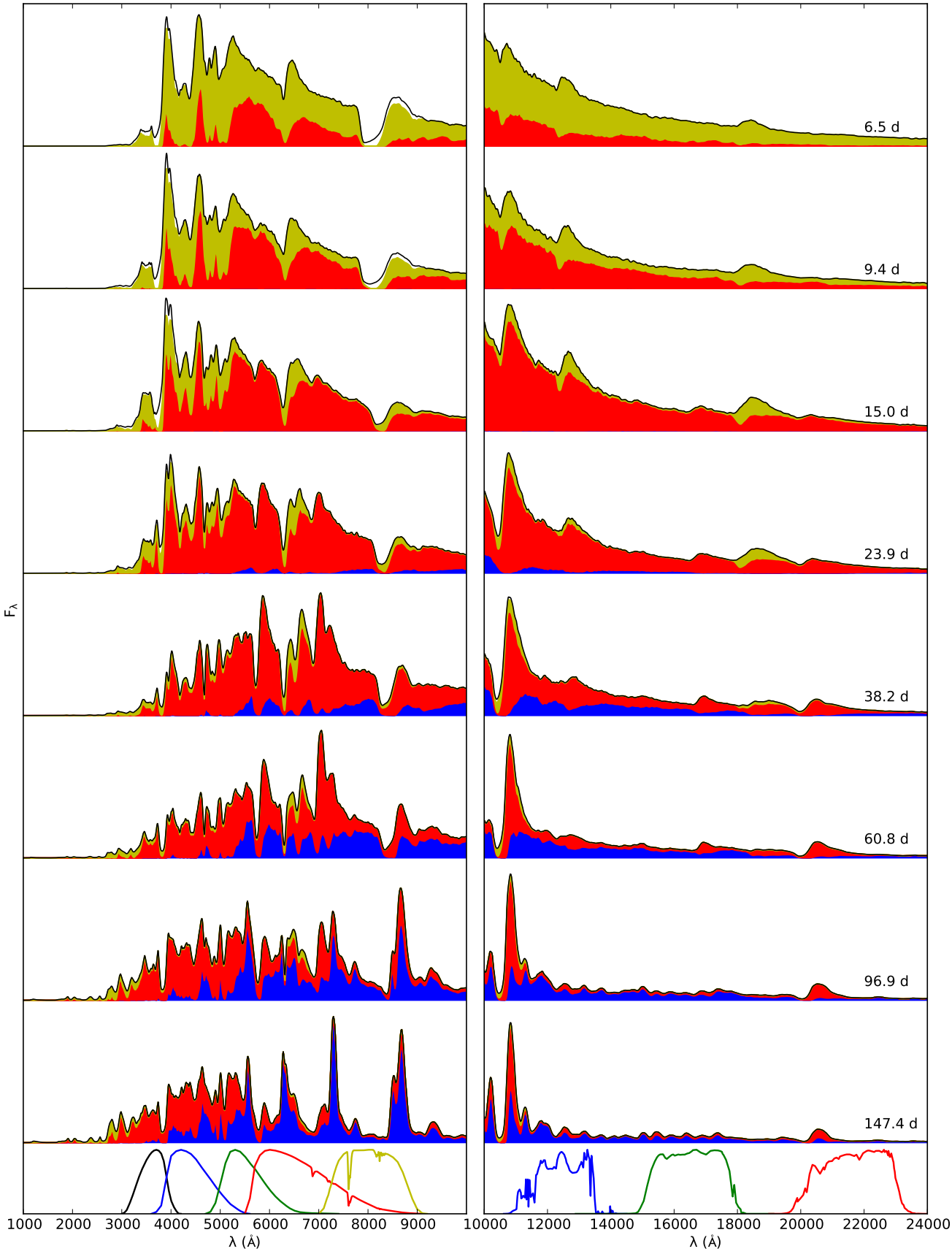

Fig. 14. Spectral evolution ine the UV+optical (left panel) and NIR (right panel) for model 12C as calculated with JEKYLL. In the spectra we show the contributions to the emission from the carbon-oxygen core (blue), and the helium (red) and hydrogen (yellow) envelopes. At the bottom we show the transmission profiles of the optical Johnson-Cousine *U* (black), *B* (blue), *V* (green), *R* (red) and *I* (yellow) bands and the NIR 2MASS *J* (blue), *H* (green) and *K* (red) bands.

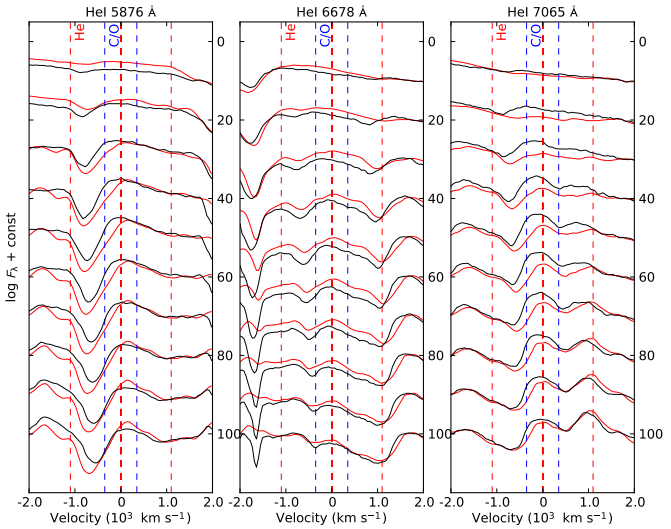

Fig. 16. Evolution of optical helium lines for model 12C as calculated with JEKYL (black) compared to the observations of SN 2011dh (red). Spectra from 10 equally spaced epochs between 10 and 100 days are shown, where those of SN 2011dh have been interpolated as decribed in E14.

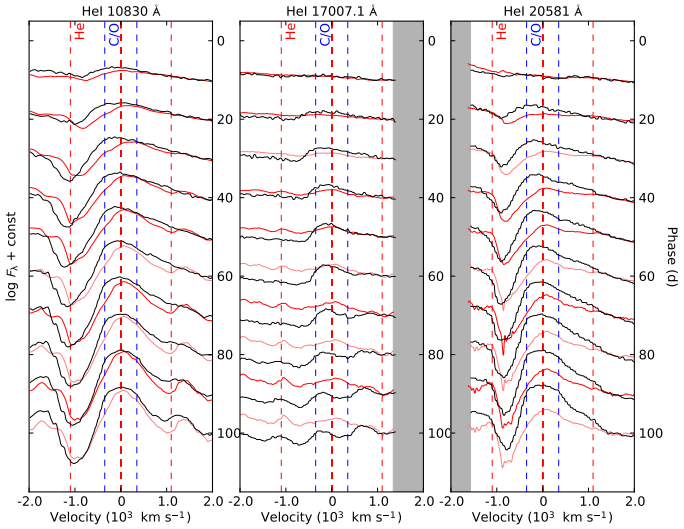

Fig. 17. Evolution of NIR helium lines for model 12C as calculated with JEKYL (black) compared to the observations of SN 2011dh (red). Otherwise as in Fig. 16.

5.2.3. Carbon-Calcium

The contribution from Carbon-Calcium lines to the model is shown in Fig. 13, and except for Calcium which contribution is strong at all times, the contribution from these elements increases after ∼40 days when the core, rich in these elements becomes increasingly transparent (see Fig. 14). Figure 18 shows the evolution of the Calcium (Ca II 3934,3968 Å, 8498,8542,8662 Å and [Ca II] 7291,7323 Å) lines as compared to SN 2011dh. In the model, the two former mainly formes in the helium envelope whereas the latter forms in the core. Expect before ∼15 days the evolution of the Calcium lines is well reproduced by the model. However, before ∼15 and ∼10 days, respectively, the absorption in the Ca II 3934,3968 Å and Ca II 8498,8542,8662 3934 Å lines extends throughout the hydrogen

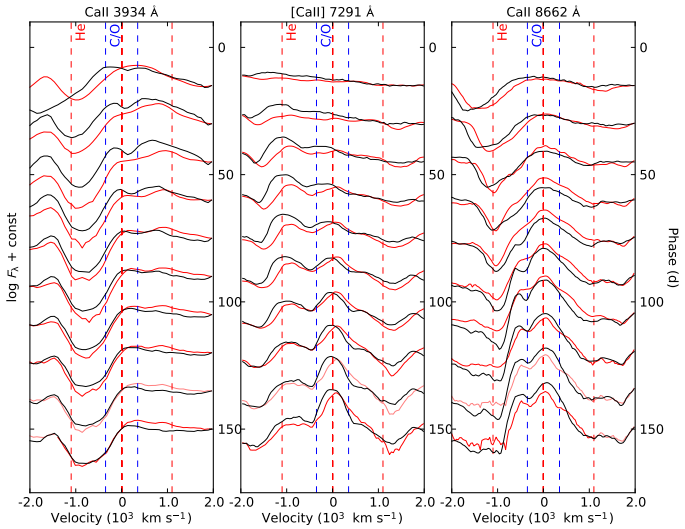

Fig. 18. Evolution of calcium lines for model 12C as calculated with JEKYL (black) compared to the observations of SN 2011dh (red). Spectra from 10 equally spaced epochs between 15 and 150 days are shown, where those of SN 2011dh have been interpolated as decribed in E14.

envelope in the model. As mentioned before, this is possibly an effect of the choice of initial conditions for the model.

Figure 19 shows the evolution of the Oxygen (O I 5577 Å, 6300,6364 Å, 7774 Å and 11290,11300 Å) and Magnesium (Mg I 15040 Å) lines as compared to SN 2011dh. In the model, these lines forms mainly in the core, although the O I 7774 Å line also have a contribution from the Helium envelope, at least to begin with. The evolution of the Oxygen lines is fairly well reproduced, but the O I 7774 and 11290,11300 Å lines appears later and is initially weaker than observed for SN 2011dh. The O I 9263 Å line is also present in the model but is blended with the [Co II] 9338,9344 Å line (see below). In the model, the early feature at ∼9200 Å is mainly caused by the Mg II 9218-9244 Å line. Later the Mg I 15040 Å line appears, although this happens later and the line is initially weaker than observed for SN 2011dh. We note that about half of the radioactive Fe/Co/He material was mixed into the Helium envelope, whereas the Oxygen and Magnesium rich material in the core was not, which may explain the early supression of several Oxygen and Magnesium lines as compared to observations. In the model, the feature emerging at ∼11800 Å after ∼60 days is mainly caused by the C I 11760 Å line, and towards ∼150 days the [C I] 8727 Å line begins to contribute significantly to the blend with the Ca II 8498,8542,8662 Å line.

5.2.4. Scandium-Manganese

The contribution from Scandium-Manganese lines to the model spectrum is shown in Fig. 13, and is dominating in the 3000-4000 Å region and strong in the 4000-5000 Å region at all times. After ∼40 days it also contributes significantly to the optical emission redwards 5000 Å. The emission is the result of scattering and flourescence in a large number of transitions and individual lines are hard to distinguish. Nevertheless, blocking caused by Scandium-Manganese lines is important for the suppression of the total emission bluewards ∼5000 Å, and in particular in the

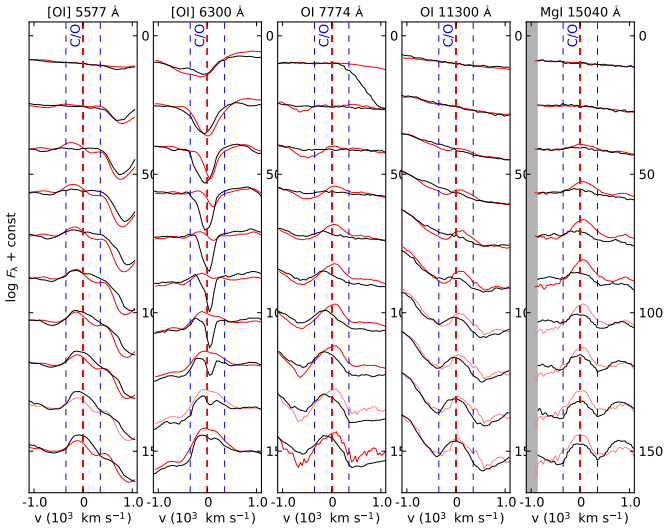

Fig. 19. Evolution of oxygen and magnesium lines for model 12C as calculated with JEKYL (black) compared to the observations of SN 2011dh (red). Otherwise as in Fig. 18.

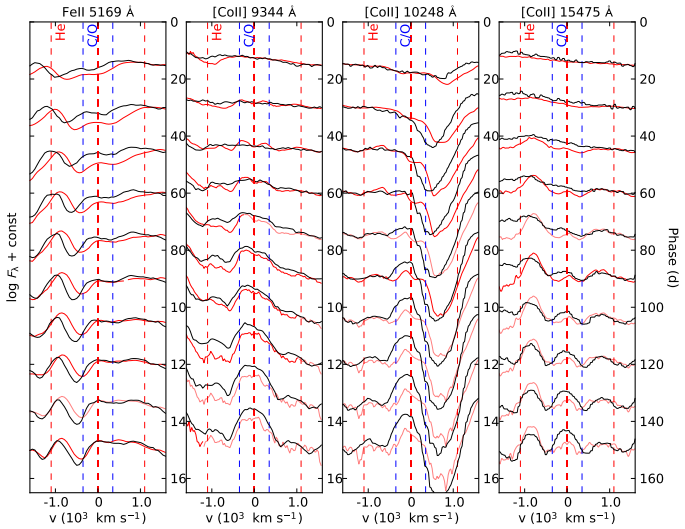

Fig. 20. Evolution of Iron and Cobalt lines for model 12C as calculated with JEKYL (black) compared to the observations of SN 2011dh (red). Otherwise as in Fig. 18.

3000-4000 Å region, corresponding roughly to the U-band (see Fig.13).

5.2.5. Iron-Nickel

The contribution from Iron-Nickel lines to the model spectrum is shown in Fig. 13, and this contribution is strong at all times, in particular in the 4000-5500 Å range. After ~40 days the contribution from Iron-Nickel increases also at other wavelenghts, likely as a consequence of the contribution from the increasingly transparent core (see Fig. 14), where about half of the Fe/Co/He material resides. Except for the U-band region (see Sect. 5.2.4), blocking through scattering and flourescence in numerous Iron lines is the main cause for the suppression of the emission bluewards ~5500 Å, so important in shaping the spectra of SE SNe. However, with a few exceptions, like the Fe II 5169 Å line, individual Iron lines are typically strongly blended and hard to distinguish. The contribution from Nickel is insignificant at all times, but after ~50 days Cobalt contributes to the spectrum with several distinct lines.

Figure 20 shows the evolution of the Iron (Fe II 5169 Å) and Cobalt ([Co II] 9338,9344 Å, 10190,10248,10283 Å and 15475 Å) lines as compared to SN 2011dh. The Fe II 5169 Å line is reasonbly well reproduced, but initially absorption occurs at higher velocities than observed, a discrepancy that disappears towards 150 days. As mentioned the [Co II] 9338,9344 Å line is blended with the O I 9338,9344 Å line, and this blend seems to be well reproduced by the model. The other [Co II] lines at 10190,10248,10283 Å and 15475 Å seems to be a bit overproduced by the model. The Iron and Cobalt lines are interesting as they are directly linked to the distribution of the Fe/Co/He material in the ejecta, and the discrepances seen may indicate that the mixing of this material is different than in the model. The absorption minimum of the Fe II 5169 Å line have been suggested a good tracer of the photosphere by several authors, and in Sect. 5.2.6 we discuss this issue as well as the distribution of the Fe/Co/He material further.

5.2.6. Line velocities

Figure 21 shows the evolution of velocity corresponding to the absorption minimum of the Hα, Hβ, He I 5876 Å, He I 6678 Å, He I 10830 Å, He I 20581 Å, and Fe II 5169 Å lines, as well as the Rosseland mean photosphere (compare; E15: Fig. 14). Towards 100 days, the Hα velocity approaches the velocity of the interface between the helium and hydrogen envelopes (11000 km s^{-1}), whereas the Hβ velocity quickly levels out near this value. Note that the high Hα velocities observed before ~10 days for SN 2011dh is not reproduced by the model, which could again be related to our choice of initial conditions. As mentioned before, in agreement whith observations, the He I 10830 Å line moves outward in velocity until ~40 days. Another interesting agreement is that the velocity saturates at a value very close to that of Hα, which in model 12C is explained by a high optical depth for this line all the way out to the interface between the helium core and the hydrogen envelope. In reasonable agreement with observations, the evolution of the He I 20581 Å velocity is almost flat at ~8000 km/s, increasing slightly towards ~40 days. The He I 5876 Å and 6678 Å velocities differs more, and the slight increase observed for the He I 5876 Å velocity towards ~40 days is not reproduced by the model.

The evolution of the Fe II 5169 Å velocity follows that of the Rosseland mean photosphere until ~30 days, confirming the claim that this line is a good tracer of the photosphere during the diffusion phase. However, as mentioned before, this velocity is higher than observed for SN 2011dh, although the discrepancy dissapears towards 150 days (see Fig, 20). It is worth noting that the Fe II 5169 Å velocity reach a plateau near ~6000 km/s, a value close to the maximum velocity for the Fe/Co/He material. This is an hint that the amount of such material mixed out in the Helium envelope could be too large, which in turn may force the photosphere to too high velocities for too long time.

5.3. Photometric evolution

Figure 22 shows the broad-band lightcurves for model 12C between 0 and 150 days as compared to observations of SN 2011dh. In agreement with observations, the maximum oc-

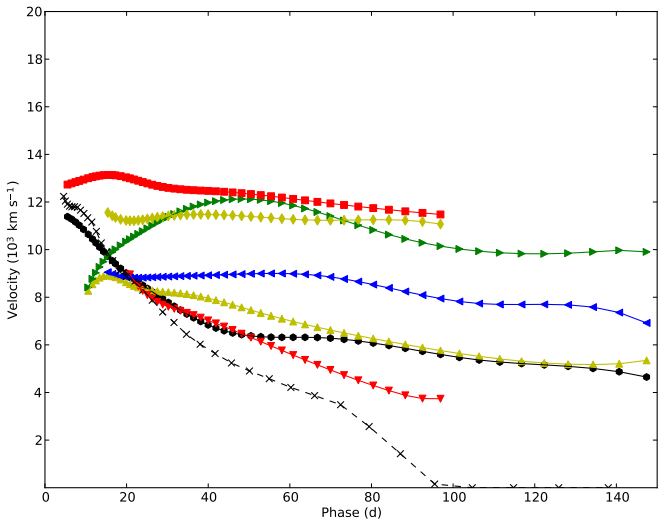

Fig. 21. Velocity evolution of the absorption minimum of the Hα (red squares), Hβ (yellow diamonds), He I 5876 Å (yellow upward triangles), He I 6678 Å (red downward triangles), He I 10830 Å (green rightward triangles), He I 20581 Å (blue leftward triangles) Å, and Fe II 5169 Å (black circles) lines for the model 12C as calculated with JEKYLL. The black crosses shows the veclocity evolution of the continuum Rosseland mean photosphere ($\tau = 2/3$).

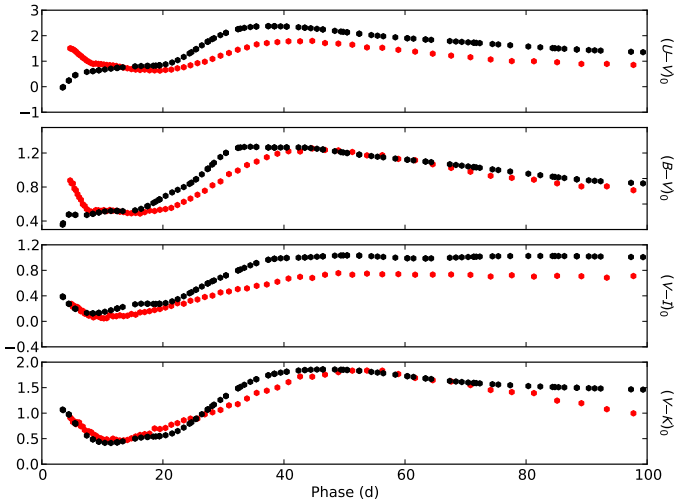

Fig. 23. $U-V$, $B-V$, $V-I$ and $V-K$ colour evolution for model 12C as calculated with JEKYLL compared to observations of SN 2011dh (red).

curs at increasingly later times for redder bands and the drop onto the tail is more pronounced (deeper and faster) for bluer bands. Also in agreement with observations, the early (before 100 days) tail decline rates are generally higher for redder bands, with the J-band lightcurve having the steepest slope and the U-band lightcurve being almost flat. As have been noted in several sample studies (i.e. Taddia et al. 2015, 2017), the former two of the lightcurve properties discussed here are shared not only by SN 2011dh, but by stripped envelope (Type IIb, Ib and Ic) SNe in general. They are also in agreement with the SE-SNe NLTE models presented by Dessart et al. (2015, 2016), and the lightcurves of the Type IIb model 3p65Ax1 are particularly similar to those of model 12 C.

Altough the overall agreement with observations is quite good, there are several differences between the model and the observations of SN 2011dh worth noting. Most notable are the differences in the U, J and K-bands and the evolution between 25 and 50 days, which is slower in R and bluer bands than observed for SN 2011dh. The growing discrepancy in the K-band could be related to dust formation in the ejecta (E15), and might suggest that this happens earlier than proposed in E15. Some of the discrepancy in the U-band could be explained by an underestimate of the extinction, but not all as the discrepancy is considerably larger on the tail than at peak.

5.4. Colour evolution

Figure 23 shows the $U-V$, $B-V$, $V-I$ and $V-K$ colour evolution for model 12C between 0 and 100 days as compared to observations of SN 2011dh. Initially, we see a blueward trend in all colours reaching a mininum at ~10 days. Subsequently all colours redden and reaches a maximum at ~40 days, in turn followed by a slow blueward trend for all colours, although the V-I colour stays almost constant. This behaviour is in agreement with observations, although there we do not observe an initial blueward trend in the $U-V$, $B-V$ colours, most likely due to influence of initial cooling tail, not present in the model due to our choice of initial conditions. As have been noted in several sample studies (i.e. Stritzinger et al. 2017), the properties of the colour evolution discussed here are shared not only by SN 2011dh, but by stripped envelope (SE; Type IIb, Ib and Ic) SNe in general. They are also in agreement with the SE-SNe NLTE models presented by Dessart et al. (2015, 2016), and the colour evolution of the Type IIb model 3p65Ax1 are particularly similar to those of model 12 C. As was noted for the lightcurve, the model evolution after ~20 days is a bit slower than observed for SN 2011dh. The model $V-I$ and $U-V$ colours are bluer than observed for SN 2011dh, reflecting the differences seen in the I- and U-bands.

5.5. Bolometric evolution

Figure 25 shows the pseudo-bolometric UV to MIR lightcurve for model 12C between 0 and 100 days as compared to observations of SN 2011dh. As for the broad-band lightcurves, the model bolometric lightcurve is not a perfect match and is broader than the observed one. This is not entirely surprising as the model was constructed by hand to fit the late nebular evolution, but it might indicate that a lower E/M ratio is needed. On the other hand the mixing of the radioactive ^{56}Ni play a stronger role when non-thermal ionization is taken into account (see Sect. 5.6), and we leave a further exploration of this, which would require a new grid of models to be constructed, for future work.

5.6. The effect of NLTE

Figures 26 and 27 shows the bolometric lightcurve and the spectral evolution of model 12C calculated with JEKYLL with and without non-thermal ionization and excitation. Before 10 days both the bolometric lightcurve and the spectral evolution are very similar, afterwhich they start to differ in several aspects. This turning point concides with the time when the radioactive energy deposition becomes important outside the photosphere (see Fig. 11). The most striking difference in the spectral evolution is the abscence of (strong) helium lines in the model without non-thermal ionization and excitation. This well-known effect was originally proposed by Lucy (1991) and have been discussed in

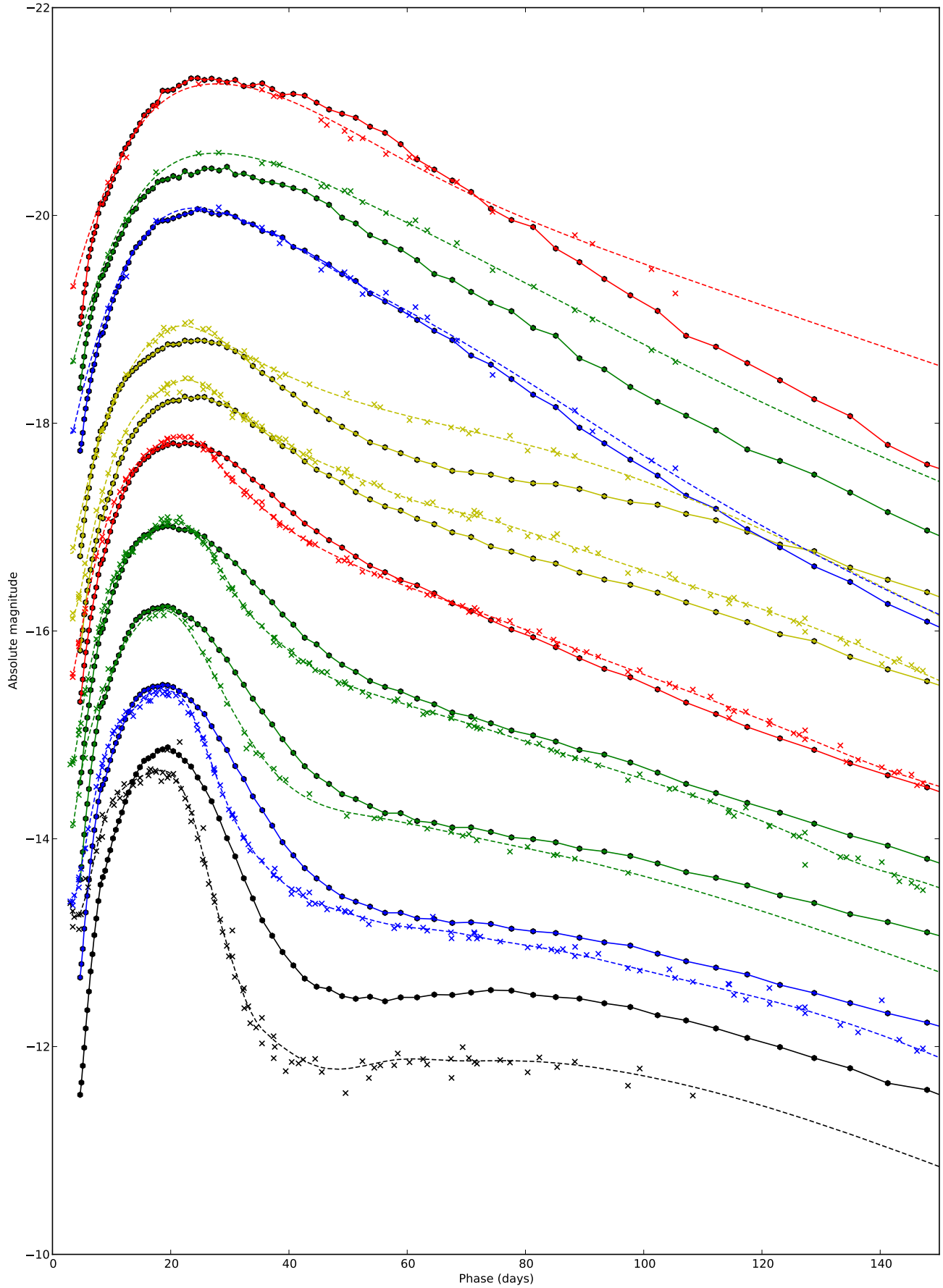

Fig. 22. Broadband optical and NIR lightcurves for model 12C as calculated with JEKYLL compared to observations of SN 2011dh

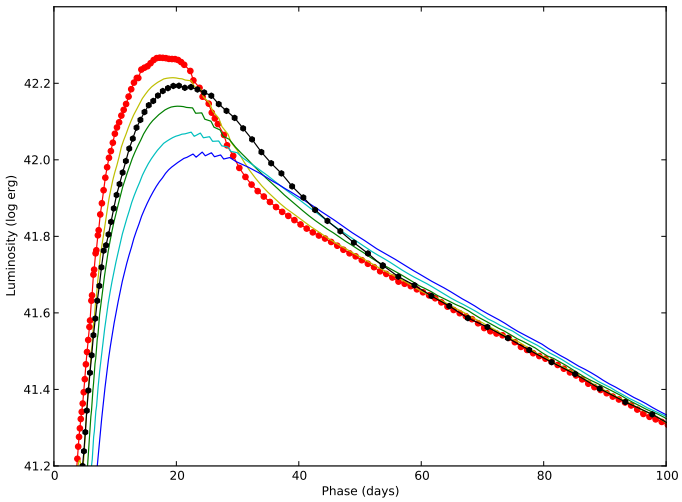

Fig. 24. Bolometric lightcurve for model 12C as calculated with JEKYLL (black circles) and the bolometric lightcurve for model 12C calculated with HYDE using an opacity floor of 0.024 (red circles), 0.05 (yellow line), 0.1 (green line) 0.15 (cyan line) and 0.2 (blue line) cm^2 g^{-1}.

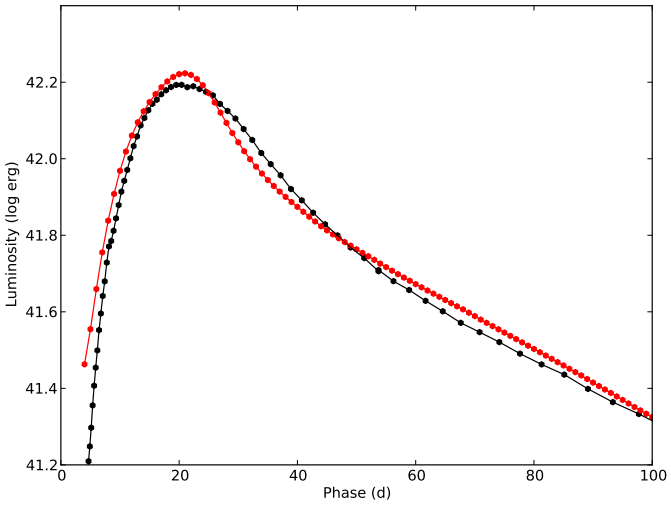

Fig. 25. Pseudo-bolometric UV to MIR lightcurve for model 12C as calculated with JEKYLL (black circles) and te observed pseudo-bolometric UV to MIR lightcurve for SN 2011dh (blue circles).

some detail by Dessart et al. (2012). Less known is the quite strong effect on the bolometric lightcurve, where the diffusion peak of the model without non-thermal ionization and excitation is considerably narrower. The reason for this seems to be the increased degree of ionization, and therefore the increased electron scattering opacity in the outer region. Contrary to Type Ia SNe (reference), the electron scattering opacity is quite important in shaping the lightcurves of Type IIb SNe, which are therefore sensitive to the degree of ionization. In Fig. 29 we also show a model calculated assuming LTE for the excited levels of the ions (but not for the ionization balance), in a manner similar to what is done by ARTIS. This model shows an even narrower bolometric lightcurve and the reason again seems to be the degree of ionization and the electron scattering opacity. In Fig. 28 we show the electron fraction in the three models near peak luminosity, which clearly supports this explanation.

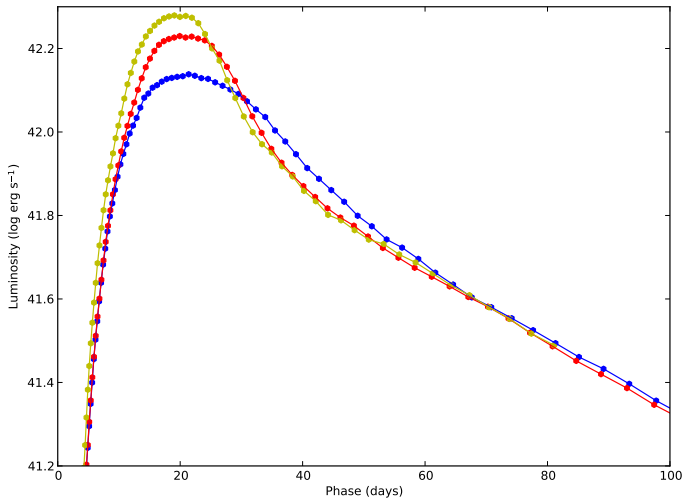

Fig. 26. Bolometric lightcurve for model 12C calculated with (blue) and without (red) non-thermal ionization and excitation. We also show a model assuming LTE for the excited levels (yellow), calculated in a manner similar to ARTIS.

In E15 we calculated the bolometric lightcurve for model 12C with the LTE-based code HYDE, and in Fig. 24 we show this lightcurve together with the one calculated by JEKYLL. HYDE use opacities calculated for a static medium in LTE, and an opacity floor intended to immitate the effects of expansion and non-thermal ionization. However, the floor was calibrated to the hydrodynamical code STELLA (Melina Bersten, private communication) which does not include non-thermal ionization, so this effect is not taken into account. Comparing the bolometric lightcurves calculated with JEKYLL and HYDE, we see that the latter is considerably narrower, in line with the comparisons discussed above. Furtermore, as also shown in Fig. 24, a good match between the JEKYLL and HYDE calculations is not possible even if the opacity floor is increased, and a more elaborate parametrization of the HYDE opacity is required. In the literature, codes similar to HYDE are commonly used to calculate bolometric lightcurves, and our results highlights the need for full NLTE calculations to properly determine the opacities.

A more detailed discussion on how non-thermal ionzation/excitation and other aspects of NLTE affect the observed evolution is outside the scope of this paper and has been postponed to a separate paper.

5.7. The effect of macroscopic mixing

Figures 29 and 30 shows the bolometric lightcurve and the spectral evolution of model 12C calculated with JEKYLL using miscroscopic and macroscopic mixing of the material. Before 15 days both the bolometric lightcurve and the spectral evolution is very similar in the two mixing scenarious, afterwich the spectral evolution becomes increasingly different. The bolometric lightcurves also differs around the peak, but once on the tail the difference becomes quite modest. The largest differences are seen in the spectral evolution in the nebular phase. In particular, the Ca II 8498,8542,8662 Å and [Ca II] 7291,7323 Å lines becomes much stronger, whereas the O I 6300,6363 Å line gets much weaker in the microscopic mixing scenario. The difference gets even worse after 150 days (not shown), and it seems clear that macroscopic mixing needs to be taken into account, at least in the nebular phase, for the model to be realistic. A more

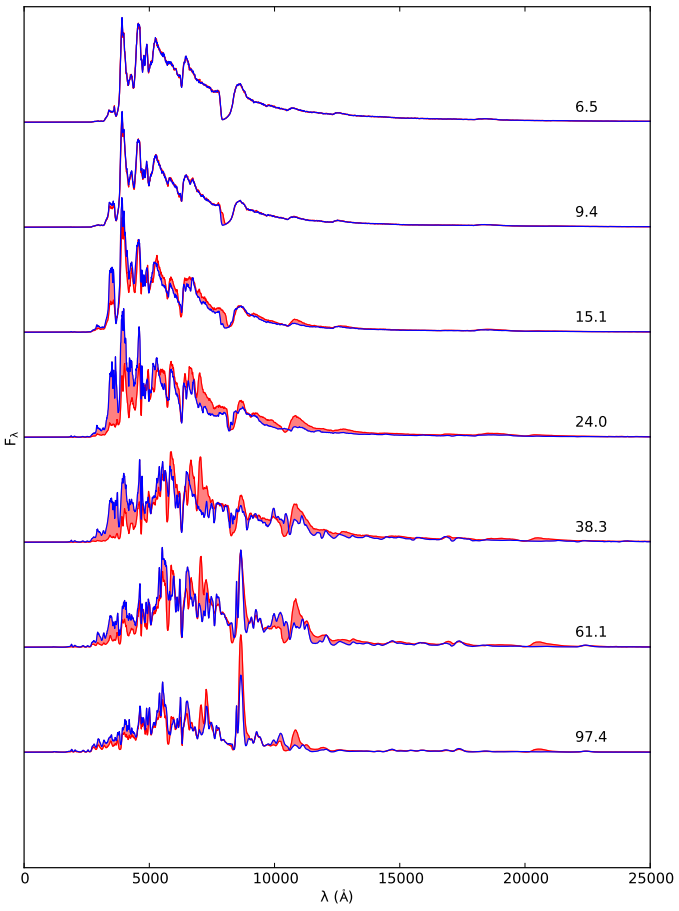

Fig. 27. Spectral evolution for model 12C calculated with (blue) and without (red) non-thermal ionization and excitation.

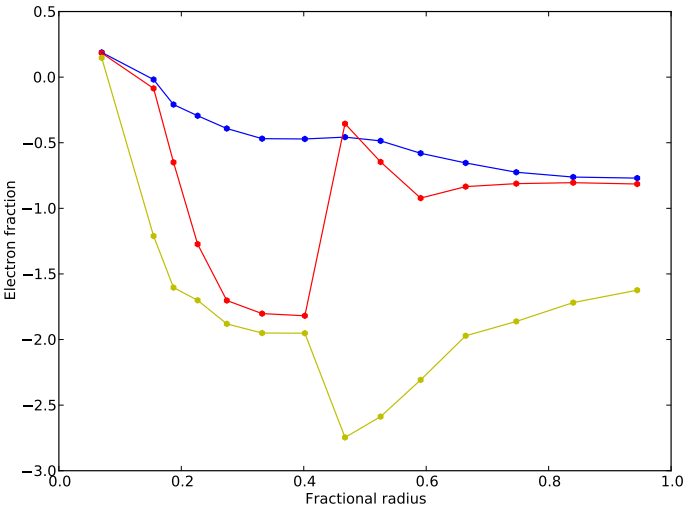

Fig. 28. Electron fraction near peak luminosity (23.5 days) for model 12C calculated with (blue) and without (red) non-thermal ionization and excitation. We also show a model assuming LTE for the excited levels (yellow), calculated in a manner similar to ARTIS.

detailed discussion on macroscopic mixing and the effects of it is outside the scope of this paper and has been postponed to a separate paper.

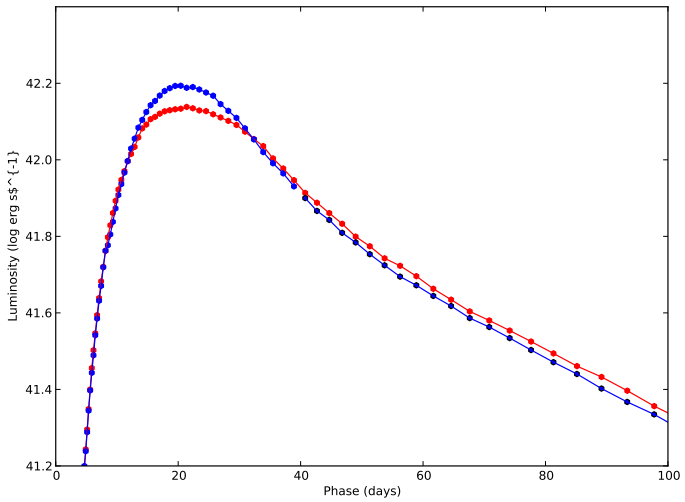

Fig. 29. Bolometric lightcurve for model 12C as calculated with JEKYLL using macroscopic (blue) and microrscopic (red) mixing.

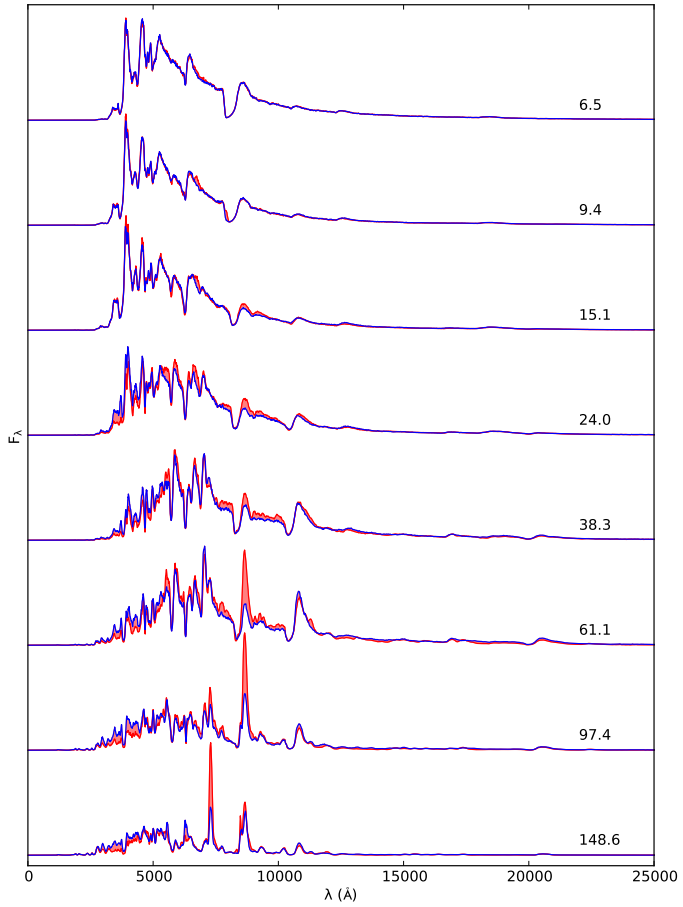

Fig. 30. Spectral evolution for model 12C as calculated with JEKYLL using microscopic (blue) and microscopic (red) mixing.

6. Conclusions

We present and described JEKYLL, a new code for modelling of SNe spectra and lightcurves. The code assumes homologues expansion, spherical symmetry and steady state for the matter, but is otherwise capable of solving for the time-evolution of the

matter and the radiation field in full NLTE. We also present comparisons with and ARTIS and SUMO, two codes that are similar to JEKYLL in some, but not all aspects. The comparisons are done with ARTIS in the photospheric phase and SUMO in the nebular phase, and they both show a good agrement in the observed quantities as well as the state variables.

We have applied JEKYLL to Type IIb SNe, by evolving the preferred J15 model for SN 2011dh through the early phase. This model, which has an initial mass of 12 $M_{\odot}$, was previously found to give a good agreement with the nebular spectra (J15) and lightcurves (E15), and here we find a resonable agreement with the early spectra and lighcurves as well. Several quantitative differences exists, however, and to find a model that improves the agreement is a challange to be adressed in future works. Nevertheless, most important observational aspects of SN 2011dh, many of which are observed in other Type IIb SNe as well, are well reproduced by the model. This demonstrates that our understanding of SN 2011dh and its progenitor star, as well as Type IIb SNe in general, have reached a mature level.

We find strong effects of NLTE as well as macroscopic mixing on the spectra and the lightcurves, which shows that both of this is necessary for realistic simulations of SNe. In particular, NLTE effects are strong even on the bolometric lightcurve, which casts some doubts on LTE-based modelling of the bolometric lightcurve commonly used in the literature. For example non-thermal ionization turns out to have a strong effect on the ionization level in the helium envelope, which introduce a coupling between the mixing of the radioactive ^{56}Ni and the diffusion time not accounted for in LTE-based models.

7. Acknowledgements

We thank Anders Jerkstrand for his invaluable help in comparing JEKYLL to his spectral code SUMO.

References

Bersten, M. C., Benvenuto, O. G., Nomoto, K., et al. 2012, ApJ, 757, 31
Dessart, L., Hillier, D. J., Li, C., & Woosley, S. 2012, MNRAS, 424, 2139
Dessart, L., Hillier, D. J., Woosley, S., et al. 2015, MNRAS, 453, 2189
Dessart, L., Hillier, D. J., Woosley, S., et al. 2016, MNRAS, 458, 1618
Ergon, M., Jerkstrand, A., Sollerman, J., et al. 2015, A&A, 580, A142
Ergon, M., Sollerman, J., Fraser, M., et al. 2014, A&A, 562, A17
Falk, S. W. & Arnett, W. D. 1977, ApJS, 33, 515
Jerkstrand, A., Ergon, M., Smartt, S. J., et al. 2015, A&A, 573, A12
Jerkstrand, A., Fransson, C., & Kozma, C. 2011, A&A, 530, A45
Kozma, C. & Fransson, C. 1992, ApJ, 390, 602
Kromer, M. & Sim, S. A. 2009, MNRAS, 398, 1809
Lucy, L. B. 1991, ApJ, 383, 308
Lucy, L. B. 2002, A&A, 384, 725
Lucy, L. B. 2003, A&A, 403, 261
Lucy, L. B. 2005, A&A, 429, 19
Maund, J. R., Fraser, M., Ergon, M., et al. 2011, ApJ, 739, L37
Mazzali, P. A. & Lucy, L. B. 1993, A&A, 279, 447
Shull, J. M. & van Steenberg, M. 1982, ApJS, 48, 95
Stritzinger, M. D., Taddia, F., Burns, C. R., et al. 2017, ArXiv e-prints
Taddia, F., Sollerman, J., Leloudas, G., et al. 2015, A&A, 574, A60
Taddia, F., Stritzinger, M. D., Bersten, M., et al. 2017, ArXiv e-prints
Verner, D. A., Ferland, G. J., Korista, K. T., & Yakovlev, D. G. 1996, ApJ, 465, 487
Verner, D. A. & Yakovlev, D. G. 1995, A&AS, 109, 125
Woosley, S. E., Eastman, R. G., Weaver, T. A., & Pinto, P. A. 1994, ApJ, 429, 300
Woosley, S. E. & Heger, A. 2007, Phys. Rep., 442, 269